Master's thesis

NTNU
Norwegian University of Science and Technology
Faculty of Natural Sciences
Department of Chemistry

Åsmund Haugen Tveten

Equilibrium geometry optimization using a multilevel Hartree-Fock wave function

Master's thesis in Applied Theoretical Chemistry
Supervisor: Ida-Marie Høyvik
June 2020

NTNU
Norwegian University of
Science and Technology

Åsmund Haugen Tveten

Equilibrium geometry optimization using a multilevel Hartree-Fock wave function

Master's thesis in Applied Theoretical Chemistry
Supervisor: Ida-Marie Høyvik
June 2020

Norwegian University of Science and Technology
Faculty of Natural Sciences
Department of Chemistry

NTNU

Kunnskap for en bedre verden

Preface

This thesis concludes my Master's Degree Programme in Chemistry (MSCHEM) with specialization in Applied Theoretical Chemistry at the Norwegian University of Science and Technology (NTNU). The project work was conducted between September 2018 and June 2020 under the supervision of Ida-Marie Høyvik.

I would like to thank my supervisor Ida-Marie Høyvik for her amazing support during these two years, in guiding me, believing in me, pushing me forward, and always being available.

I would also like to thank Eirik Kjønstad for his much-needed help with the programming work that went into this project.

A big thanks also goes to my friends and my brother for making these past few months much more enjoyable through social activities online. Finishing a thesis amidst the coronavirus pandemic lockdown would have been depressing without you.

Lastly, I would like to thank my parents for their endless love and support, and their stream of phone calls cheering me on.

Thank you.

Sammendrag

Optimering av likevektsgeometrier er et viktig trinn i studiet av diverse molekylære egenskaper. Mangle slike egenskaper er lokale, hovedsaklig knyttet til en liten region av det totale molekylære systemet. Dette gjør multilevel-metoder passende for beregning av lokale egenskaper, ettersom disse metodene modellerer ulike regioner på ulike nivå av teori, og derav tillater nøyaktige beskrivelser av regionen man er interessert i til redusert beregningskostnad. Denne avhandlingen ser på en nylig introdusert multilevel Hartree-Fock (MLHF) metode, og videreutvikler denne metoden for optimering av likevektsgeometrier. MLHF-metoden er en to-nivå-metode, som modellerer den aktive regionen med en HF-optimert tetthet og den inaktive regionen med et startgjett for tettheten. Den molekylære gradienten for MLHF utledes analytisk, og implementeres på en slik måte at den inaktive regionen er frosset i rommet mens geometrien optimeres. Implementering og testing av metoden utføres i det nylig utgitte elektronstrukturprogrammet eT. Likevektsgeometrier for fire små testsystemer beregnes og undersøkes i forhold til energi og et utvalg av bindingslengder og bindingsvinkler. Sammenlignet med HF-optimerte geometrier er MLHF-geometriene høyere i energi, med en energiforskjell på størrelsesorden 10^{-2} Hartree eller mindre. Videre sammenligninger gjøres med HF-geometrier der den samme regionen som var frosset for MLHF-beregningen også fryses for HF-beregningen. MLHF-geometriene er forsatt høyere i energi en disse "frossen-HF"-geometriene, men forskjellene er kun på størrelsesorden 10^{-3} Hartree. Forskjellene i de utvalgte bindingslengdene og bindingsvinklene for disse to metodene er innenfor henholdsvis 2.8 pm og 2.6°. Dette er innenfor de vanlige intervallene for feil på HF-nivået av teori, og til gjengjeld gir MLHF-metoden en kraftig reduksjon i antall orbitaler som inngår i optimeringen. Effekten av å utvide det MLHF-aktive rommet utover den ikke-frosne regionen undersøkes, og de korresponderende geometriene nærmer seg ikke frossen-HF-geometrien. Dette motstrider hva som er forventet, og kan muligens skyldes en forglemmelse i implementeringen, men ingen definitiv forklaring er blitt funnet. Resultatene som er blitt oppnådd kommer bare fra små systemer, og sammenlignes kun innenfor HF-nivået av teori. Disse begrensningene for resultatene må riktignok huskes på, men MLHF geometrioptimering virker likevel lovende når det gjelder utsikter for bruk på store systemer, og for å fungere som et startpunkt for nøyaktige korrelerte metoder. Et av leddene i den molekylære MLHF-gradienten er beregningsmessig kostbart, og kan representere en utfordring for utviklingen av en effektiv implementering av metoden. Et par approksimasjoner til dette leddet utprøves, basert på enkle approksimative oppdateringsalgoritmer, men det viser seg at de introduserer en alvorlig forstyrrelse i gradienten, hvilket gjør dem ubrukelige.

Abstract

The optimization of equilibrium geometries is an important step in the study of various molecular properties. Many such properties are local, connected mostly to a small region of the entire molecular system. This makes multilevel methods appropriate for the calculation of localized properties, as these methods model different regions at different levels of theory, allowing accurate descriptions of the region of interest at reduced computational cost. This thesis concerns a recently introduced multilevel Hartree-Fock (MLHF) method, and develops this method for equilibrium geometry optimization. The MLHF method is a two-level method, modelling the active region with a HF optimized density and the inactive region with the starting guess density. The MLHF molecular gradient is analytically derived, and implemented in such a way that the inactive region is frozen in space during the geometry optimization. The implementation and testing of the method is done in the newly released electronic structure program eT. Equilibrium geometries of four small test systems are obtained and investigated in terms of energy and a selection of bond lengths and bond angles. When compared with HF optimized geometries, the MLHF geometries are higher in energy, with energy differences on the order of 10^{-2} Hartree or less. Further comparisons are made to HF optimized geometries where the same region that was frozen in space for the MLHF calculation is also frozen for the HF calculation. The MLHF geometries are still higher in energy than these "frozen HF" geometries, but the differences are only on the order of 10^{-3} Hartree. The differences in the selection of bond lengths and bond angles for these two methods are within 2.8 pm and within 2.6°, respectively. This is within the usual error bounds of the HF level of theory, and in return the MLHF method gives a large reduction in the number of orbitals used in the optimization. The effect of extending the MLHF active space beyond the unfrozen region is explored, and the corresponding geometries fail to approach the frozen HF geometry. This is contrary to what is expected, and might be the result of an oversight in the implementation; however, no conclusive explaination has been determined. The results obtained are only from small systems, and are compared only within the HF level of theory. While these limitations of the results must be kept in mind, the MLHF geometry optimization nevertheless appears promising for the prospect of application on large systems and providing a starting point for accurate correlated methods. One of the MLHF molecular gradient terms is computationally expensive and could pose a challenge for the efficient implementation of the method. A couple of approximations to this term are attempted, based on simple approximate updating schemes, but they are found to introduce a severe disturbance in the gradient, which makes them unusable.

Contents

1 Introduction

During the last six decades, computational chemistry has become an indispensable tool in numerous areas of research. The ability to model chemical structures and processes at the molecular level opens up the possibility to understand properties and phenomena such as molecular structure, electronic structure, energy levels, vibrational frequencies, magnetic responses, and reaction mechanisms, in ways not accessible through laboratory experiments. These computational models thus aid the research in important areas like the study of biological systems, organic synthesis, and material sciences, and help to guide experimental procedures in the search for and development of new drugs, efficient catalysts, or novel functional materials.

Within computational chemistry, the field of *geometry optimization*[1] concerns the study of molecular properties and phenomena related to the geometric structure of molecular systems, and the responses to perturbations of this structure. Often, this will involve constructing and investigating the *potential energy surface* (PES) of the system. The PES represents the electronic energy as a multivariable function of all nuclear geometrical coordinates, providing at each distinct molecular geometry the corresponding energy. The study of the PES concerns problems such as locating stationary points and lowest-energy-pathways, corresponding to important geometrical properties like equilibrium geometries, transition states, and reaction paths. As the PES is a complicated surface, locating a stationary point is not a one-step process, but must be done in an iterative fashion where an approximate step is calculated in each iteration. Ideally, this process will converge to the stationary point as more and more steps are taken. One of the most popular among such iterative methods is *Newtons method*, which approximates the PES locally by a quadratic function and calculates the step using the *molecular gradient* (matrix of first derivatives) and *molecular Hessian* (matrix of second derivatives). In any geometry optimization, the molecular gradient and Hessian are also used to confirm and characterize the stationary points. A point is stationary if the corresponding gradient is zero, and can be further characterized as a minimum, maximum, or saddle point by inspecting the structure of the Hessian. This thesis will focus on finding equilibrium geometries, corresponding to PES minima.

The construction of the PES is made possible by applying the *Born-Oppenheimer approximation*. It states that because of the large difference in mass between an electron and a nucleus, and the consequently large difference in their movement speed, the assumption that the motion of the electrons in a molecule can be treated separately from the motion of the nuclei is reasonable. This allows us to treat the electronic structure with a parametric dependence on the nuclear positions, and obtain a distinct electronic structure at each geometry. Being able to focus our attention on the motion of the electrons is pivotal not only because a majority of chemical phenomena are intimately linked to electronic structure specifically, but because the treatment of electronic structure is an intricate one. The underlying theory of motion in a molecular system is quantum mechanics (QM), in which the properties of the system are contained in the quantum mechanical *wave function*. Models based on QM, like the *Wave Function Theory* (WFT) and *Density Functional Theory* (DFT) models, are called the *ab initio* (latin: "From first principles")

methods. In contrast, *Molecular Mechanics* (MM) methods use classical mechanics to model the motion of the particles. In the WFT methods, the wave function is obtained by solving the Schrödinger equation. Under the Born-Oppenheimer approximation, a distinct electronic wave function can be obtained at each molecular geometry. Unfortunately, for systems with more than one electron, the equation cannot be solved analytically for the exact electronic wave function. It is however possible to construct approximate wave functions, and one very important method for doing so is the *Hartree-Fock* (HF) method. This method models each electron as feeling an averaged potential of all the other electrons in the system, as opposed to treating all distinct electron-electron interactions. This has led to the definition of *electron correlation energy* as the difference between the exact ground-state energy and the energy given by HF in the limit of a complete basis[2]. Despite HF giving energies typically within 1% of the exact energies, the lack of electron correlation energy means that it is not possible to obtain quantitative results with HF alone[3]. Where higher accuracy is needed, HF is commonly used as a starting point for more accurate WFT methods like *Møller-Plesset Perturbation Theory* (MP), *Configuration Interaction* (CI), and *Coupled Cluster* (CC)[2]. These post-HF methods introduce hierarchies of improvements to the HF wave function as a way to systematically include more and more of the electron correlation energy. The higher accuracy unfortunately comes with the price of larger computational cost. For example, the full CI method, which is exact within a given basis set, scales exponentially with the size of the system, while the highly accurate *Coupled Cluster Singles Doubles Triples* (CCSDT) method formally scales with the 8th power of the size of the system[2]. These kinds of fast scalings put a severe limit on the system sizes to which these accurate methods can by applied. In particular, the large computational cost is prominent in geometry optimizations, where the optimization of the wave function and energy is required in each of the geometry iterations.

In short, the problem of high computational cost arises when we require a fast-scaling method applied to a large molecular system in order to get acceptable results. However, even when highly accurate estimates of a molecular property are needed, it seems unlikely that the entirety of a large system should need to be described at the same degree of accuracy. This applies especially when studying properties that are connected mostly to a smaller subsystem, a classic example being the study of enzymes and enzymatic catalysis, where activity occurs in the small active site of the enzyme[4,5]. Clearly, it would be highly desirable to be able to divide a system into different regions and model them at different degrees of accuracy, in a way that reduces computational cost while still yielding acceptable results. The *multi-level methods*, also known as *embedding methods*, exist precisely for this purpose. These come in a variety of families like the hybrid QM/MM methods[4] which couple accurate QM for the active region with computationally cheaper MM for the surrounding environment, the continuum solvation methods[6] which model the environment as a continuous medium rather than as discrete molecular entities, and the DFT-in-DFT[7], WFT-in-DFT[8], and WFT-in-WFT[9] methods, which couple different levels of QM theory.

The QM/MM methods were introduced by Warshel and Levitt in 1976[10], and have since been widely established for many applications such as the study of biological, inorganic, organometallic, and solid-state systems[11]. The ONIOM model introduced

by Svensson *et al.*[12] in 1996 is particularly flexible, allowing multiple layers with different QM and MM models. In QM/MM methods, covalent bonds between the regions are cut, and the use of link atoms to cap these bonds is required[13]. For geometry optimizations, QM/MM often employ a so-called microiteration scheme where at each iteration of the QM region optimization, the MM region is fully and inexpensively optimized; however, including the electrostatic interactions between the QM and MM region has been somewhat challenging for this approach[13]. In DFT-in-DFT and WFT-in-DFT methods, the coupling between the two levels of theory is described by a so-called embedding operator, which generally consists of a classical electrostatic component as well as a nonlocal component arising from the Pauli principle[14]. The construction of this embedding operator is not at all trivial, and many different strategies have been developed for this purpose[14–17]. Continuum solvation methods are important for the modelling of solvated systems[6,18], since the uniform solvent environment is well represented by a continuum. The effects of a solute on the continuum can be easily represented by a QM operator, making it straightforward to couple the continuum with a QM description of the solute[19]. Notable continuum models include the *Polarizable Continuum Model* (PCM)[20] and the *Conductor-like Screening Model* (COSMO)[21].

While the importance of DFT, MM, and continuum models in computational chemistry is undeniable, these methods will not be discussed further, and our focus will instead be on the WFT methods. WFT-in-WFT multilevel methods are less common than QM/MM and DFT-in-DFT. Notable examples include the CC-in-CC model by Höfener and Visscher[9], the hybrid model by Mata *et al.*[22], and the cluster-in-molecule model by Li and Piecuch[23], which was later combined with frozen natural orbitals by Rolik and Kállay[24]. Most such multilevel post-HF methods need to be provided with an already optimized HF wave function, which will be expensive for large systems. In 2014, Myhre *et al.*[25] presented a general scheme for coupling multiple layers of different level CC for which the Pauli-principle is fulfilled across all borders.

This thesis will concern a recent multilevel Hartree-Fock (MLHF) model developed in the master thesis of Dundas[26] under the supervision of Høyvik, later reformulated in the molecular orbital (MO) basis by Sæther *et al.*[27]. It models the entire system by a single Slater determinant MLHF wave function, thus introducing no bond breaking or neglection of interactions at the boundaries. The MO basis formulation is able to exploit a significant reduction in matrix dimensions compared to the atomic orbital (AO) dimension. It may therefore be used as a cheaper starting point for post-HF multilevel methods than a full-space optimized wave function as mentioned earlier. The model was indeed used as a starting point for CCSD in the master thesis of Sæther[28] under the supervision of Høyvik. In all of these studies, the MLHF model was implemented in local versions of the seasoned electronic structure program LSDALTON[29]. Recently, a new open source electronic structure program by the name of eT[30] was released which features this MLHF model. The eT program was developed by Folkestad and Kjønstad and collaborators at the Norwegian University of Science and Technology. In this thesis, the MLHF method has been further developed for geometry optimization by deriving the molecular gradient in the AO basis. The gradient has been implemented into a local version of the eT program, and by combining its MLHF wave function module and geometry optimization

module, AO basis MLHF geometry optimization calculations could be performed. The immobilization of the environment region has been explicitly enforced through a manipulation of the gradient referred to as the *frozen atoms* approach.

The derivation of the molecular gradient was essential for this thesis because *ab initio* geometry optimizations in general employ analytical gradients rather than using numerical differentiation. Analytical gradients have been shown to not only be more efficient, but also provide higher numerical accuracy [31,32]. The MLHF gradient gives rise to a term involving two-electron interactions in the inactive region whose construction represent a computationally expensive step. Some effort into the analysis and approximation of this term has been attempted in this work and will be presented.

In contrast to the use of analytical gradients, Hessians are usually approximated, as the construction and inversion of exact Hessians is very expensive. The *quasi-Newton methods* calculate the Newton step using an approximate Hessian which is updated in each iteration based on the energy and gradient. The *Broyden-Fletcher-Goldfarb-Shanno* (BFGS) [1] method is one of the most popular Hessian updating schemes for minimizations, but is unfit for locating saddle points [33]. Other updating schemes include the *Symmetric Rank One* (SR1) [34] and the *Powell-symmetric-Broyden* (PSB) [1] methods. The Newton equations may also be solved by applying a version of the *Direct Inversion in the Iterative Subspace* (DIIS) technique by Pulay [35] to the geometry optimization problem, an approach known as GDIIS [36], where the new geometry is obtained as a linear combination of previous geometries which minimizes the Newton step [1]. Another popular method is the *Rational Function* (RF) method, which replaces the quadratic approximation of the Newton method with a rational function approximation [33]. The choice of Hessian updating is just one of several factors which can affect the optimization performance. The choice of the *initial* Hessian, which the updating schemes do not provide, can have a great impact on the convergence since a better starting Hessian produces better approximate Hessians in the subsequent steps. Working in a suitable internal coordinate system can also significantly improve the efficiency. Properly devised internal coordinates often perform better than the simple but highly coupled Cartesian coordinates [1,33]. Finally, some form of step control to monitor and restrict the step size is usually a good idea. This thesis has not been concerned with comparing the performance of different Hessian updates, starting Hessians, and coordinate systems. The eT program, being in its earliest stage of release, does not yet offer a variety of such features in its geometry optimization module. The module currently offers only the RF method with BFGS Hessian updating and a scaled identity matrix initial Hessian in Cartesian coordinates. Rather, the aim has been to achieve MLHF geometry optimization functionality fit for proof-of-concept calculations with little regard for efficiency at this stage. Still, having an idea of how different factors may affect the performance is instructive.

This thesis is structured as follows. Chapter 2 presents some background theory of the density-based HF energy optimization, the extension to the multilevel analogue, and second order geometry optimization. Chapter 3 presents the derivation of the MLHF molecular gradient, followed by the design of two approximations to the expensive two-electron interaction term, and lastly a method to examine this

gradient term numerically. Chapter 4 details the implementation of the MLHF geometry optimization and the frozen atoms technique into eT, the specifics of the proof-of-concept calculations, as well as the implementation of the approximate gradient terms. In Chapter 5, the results of the proof-of-concept calculations, the performance of the approximate gradient terms, and the investigation of the exact gradient term are presented and discussed. Finally, Chapter 6 gives a concluding summary, while future work is discussed in Chapter 7.

2 Background theory

2.1 Exponential parametrization

The objective of this thesis is to develop and test equilibrium geometry optimization using a multilevel Hartree-Fock (MLHF) wave function method. The geometry is moved in iterative steps until a minimum is reached, and at each new geometry the corresponding minimized energy is obtained by optimizing the wave function at that geometry. Both the minimization of the energy and the optimization of the geometry will be carried out in the *density formulation* of HF theory. In this formulation, electronic states are represented by *density matrices* $\mathbf{D}$ rather than by occupation number vectors $|\mathbf{k}\rangle$ in the Fock space. The specifics of the density formulation will be covered as part of Section 2.2, and the current section will instead concern how to carry out a transformation from one density matrix to another. Such transformations will feature heavily in both the theory of energy minimization and of geometry optimization, as the starting density will undergo changes in both of these procedures. In the energy minimization, this change is a result of varying the electronic state to look for the lowest energy. In the geometry optimization, it is a result of perturbing the molecular structure of the system. This section will present the main points of the *exponential parametrization* method, which provides a convenient way to transform between different densities.

Let $\mathbf{D}^{\mathrm{mo}}$ be a real density matrix in the molecular orbital (MO) basis. In order to constitute a valid density matrix, $\mathbf{D}^{\mathrm{mo}}$ must fulfill the *symmetry*, *trace*, and *idempotency* conditions:

$$\begin{aligned} (\mathbf{D}^{\mathrm{mo}})^{\mathrm{T}} &= \mathbf{D}^{\mathrm{mo}} \\ \mathrm{Tr}[\mathbf{D}^{\mathrm{mo}}] &= \frac{1}{2} N_{\mathrm{e}} \\ (\mathbf{D}^{\mathrm{mo}})^2 &= \mathbf{D}^{\mathrm{mo}}, \end{aligned} \tag{2.1}$$

where N_{e} is the number of electrons in the system. An arbitrary transformation of a valid density matrix will in general not result in a new density that is also valid. However, a *unitary transformation*

$$\mathbf{D}^{\mathrm{mo}} = \mathbf{U}^{\mathrm{T}} \mathbf{D}_0^{\mathrm{mo}} \mathbf{U} \tag{2.2}$$

will preserve the symmetry, trace, and idempotency of a valid reference density matrix $\mathbf{D}_0^{\mathrm{mo}}$. Here, $\mathbf{U}$ is an orthogonal matrix (which is the real analogue of a unitary matrix). In fact, any valid density may be generated from any other valid reference density by such a transformation[3]. Furthermore, any orthogonal matrix may be written as the matrix exponential of an antisymmetric matrix (the real analogue of an antihermitian matrix), and conversely the exponential of any antisymmetric matrix is orthogonal[37]. We can make use of this fact to rewrite equation 2.2 as

$$\mathbf{D}^{\mathrm{mo}}(\boldsymbol{\kappa}) = \exp(-\boldsymbol{\kappa}) \mathbf{D}_0^{\mathrm{mo}} \exp(\boldsymbol{\kappa}) \tag{2.3}$$

where $\boldsymbol{\kappa}$ is antisymmetric, i.e.

$$\boldsymbol{\kappa}^{\mathrm{T}} = -\boldsymbol{\kappa}. \tag{2.4}$$

The fact that

$$\mathbf{U} = \exp(\boldsymbol{\kappa}) \quad \Rightarrow \quad \mathbf{U}^{\mathrm{T}} = \exp(-\boldsymbol{\kappa}) \tag{2.5}$$

is easily seen from the definition of the matrix exponential:

$$\exp(\mathbf{A}) = \sum_{n=0}^{\infty} \frac{\mathbf{A}^n}{n!}. \tag{2.6}$$

The advantage of the exponential formulation in equation 2.3 is that it is simpler to work with the exponential of an antisymmetric matrix than with an orthogonal matrix directly. Antisymmetric matrices are trivial to represent by a set of independent parameters; e.g. the lower triangular part of $\boldsymbol{\kappa}$ may be chosen as independent parameters, and the remaining elements are then easily generated from the antisymmetry condition[37]. Since each element of the lower triangular part corresponds to exactly one independent parameter, $\boldsymbol{\kappa}$ will have $\frac{1}{2}N_{ao}(N_{ao}-1)$ independent parameters (where N_{ao} is the number of AOs). This method of performing a unitary transformation using the matrix exponential of an antisymmetric matrix is what is known as exponential parametrization.

If we expand equation 2.3 in terms of the definition of the matrix exponential (equation 2.6), we arrive at a representation for the exponential parametrization known as the *Baker-Campbell-Hausdorff* (BCH) expansion:

$$\begin{aligned} \mathbf{D}^{\mathrm{mo}}(\boldsymbol{\kappa}) &= \exp(-\boldsymbol{\kappa})\mathbf{D}_0^{\mathrm{mo}}\exp(\boldsymbol{\kappa}) \\ &= \mathbf{D}_0^{\mathrm{mo}} + [\mathbf{D}_0^{\mathrm{mo}}, \boldsymbol{\kappa}] + \frac{1}{2!}[[\mathbf{D}_0^{\mathrm{mo}}, \boldsymbol{\kappa}], \boldsymbol{\kappa}] + \frac{1}{3!}[[[\mathbf{D}_0^{\mathrm{mo}}, \boldsymbol{\kappa}], \boldsymbol{\kappa}], \boldsymbol{\kappa}] + \ldots \end{aligned} \tag{2.7}$$

The BCH expansion will prove essential in later sections when evaluating derivatives of the density to derive the electronic and molecular gradient.

A problem arises with the exponential parametrization in that for some $\boldsymbol{\kappa}$, the transformation yields no change to the reference density:

$$\exp(-\boldsymbol{\kappa})\mathbf{D}_0^{\mathrm{mo}}\exp(\boldsymbol{\kappa}) = \mathbf{D}_0^{\mathrm{mo}}. \tag{2.8}$$

This is referred to as a *redundant rotation* of the density. Including these redundant rotations is not only unnecessary, but may even lead to problems with convergence since they introduce singularities in the Hessian at stationary points[3]. The redundant rotations can be identified and removed by considering the *projections* of $\boldsymbol{\kappa}$. We start by noting the structure of the MO density matrix:

$$\mathbf{D}^{\mathrm{mo}} = \begin{array}{c} \\ o \\ v \end{array} \begin{array}{c} \begin{array}{cc} o & v \end{array} \\ \begin{pmatrix} \mathbf{1} & \mathbf{0} \\ \mathbf{0} & \mathbf{0} \end{pmatrix} \end{array} \tag{2.9}$$

The matrix has ones along the diagonal of the first $\frac{1}{2}N_{\mathrm{e}}$ (corresponding to the number of doubly occupied orbitals) columns and zeros elsewhere. The reason for this

structure is explained in section 2.2. Importantly, since $\mathbf{D}_0^{\mathrm{mo}}$ only has eigenvalues 1 and 0, it constitutes a *projector*[3]. Defining the projectors

$$\mathbf{P}^{\mathrm{mo}} = \mathbf{D}_0^{\mathrm{mo}} \tag{2.10}$$

and

$$\mathbf{Q}^{\mathrm{mo}} = \mathbf{I} - \mathbf{D}_0^{\mathrm{mo}} = \begin{array}{c} \\ o \\ v \end{array} \begin{array}{c} \begin{array}{cc} o & v \end{array} \\ \begin{pmatrix} \mathbf{0} & \mathbf{0} \\ \mathbf{0} & \mathbf{1} \end{pmatrix} \end{array}, \tag{2.11}$$

where $\mathbf{I}$ is the identity matrix, we have the relations

$$\mathbf{P}^{\mathrm{mo}}\mathbf{Q}^{\mathrm{mo}} = \mathbf{Q}^{\mathrm{mo}}\mathbf{P}^{\mathrm{mo}} = 0 \tag{2.12}$$

and

$$\mathbf{P}^{\mathrm{mo}} + \mathbf{Q}^{\mathrm{mo}} = \mathbf{I}. \tag{2.13}$$

Equation 2.13 allows $\boldsymbol{\kappa}$ to be written in terms of its projections as

$$\begin{aligned} \boldsymbol{\kappa} &= (\mathbf{P}^{\mathrm{mo}} + \mathbf{Q}^{\mathrm{mo}})\boldsymbol{\kappa}(\mathbf{P}^{\mathrm{mo}} + \mathbf{Q}^{\mathrm{mo}})^{\mathrm{T}} \\ &= \mathbf{P}^{\mathrm{mo}}\boldsymbol{\kappa}(\mathbf{P}^{\mathrm{mo}})^{\mathrm{T}} + \mathbf{P}^{\mathrm{mo}}\boldsymbol{\kappa}(\mathbf{Q}^{\mathrm{mo}})^{\mathrm{T}} + \mathbf{Q}^{\mathrm{mo}}\boldsymbol{\kappa}(\mathbf{P}^{\mathrm{mo}})^{\mathrm{T}} + \mathbf{Q}^{\mathrm{mo}}\boldsymbol{\kappa}(\mathbf{Q}^{\mathrm{mo}})^{\mathrm{T}}. \end{aligned} \tag{2.14}$$

The right-hand side terms correspond to the occupied-occupied, occupied-virtual, virtual-occupied, and virtual-virtual blocks of $\boldsymbol{\kappa}$, respectively. By using the idempotency of $\mathbf{D}^{\mathrm{mo}}$ and equation 2.12, it is easily shown that

$$\begin{aligned} [\mathbf{D}_0^{\mathrm{mo}}, \mathbf{P}^{\mathrm{mo}}\boldsymbol{\kappa}(\mathbf{P}^{\mathrm{mo}})^{\mathrm{T}}] &= 0 \\ [\mathbf{D}_0^{\mathrm{mo}}, \mathbf{Q}^{\mathrm{mo}}\boldsymbol{\kappa}(\mathbf{Q}^{\mathrm{mo}})^{\mathrm{T}}] &= 0. \end{aligned} \tag{2.15}$$

Thus, for the occupied-occupied and virtual-virtual blocks of $\boldsymbol{\kappa}$, all terms of the BCH expansion (equation 2.7) except the first term will vanish, resulting in no changes to the density. Therefore, the redundant rotations are the occupied-occupied and the virtual-virtual rotations, and can be removed by requiring that $\boldsymbol{\kappa}$ satisfies the projection relation

$$\boldsymbol{\kappa} = \mathbf{P}^{\mathrm{mo}}\boldsymbol{\kappa}(\mathbf{Q}^{\mathrm{mo}})^{\mathrm{T}} + \mathbf{Q}^{\mathrm{mo}}\boldsymbol{\kappa}(\mathbf{P}^{\mathrm{mo}})^{\mathrm{T}}. \tag{2.16}$$

2.2 The density based Hartree-Fock method

This section will give an overview of the theory of density based HF for energy minimization. In other words, how to optimize the HF wave function at a given molecular geometry. This will serve as a foundation on which the extension to the multilevel HF method will be presented later (section 2.3).

Our system is assumed to be nonrelativistic, and the Born-Oppenheimer approximation is applied. We will consider only closed-shell HF-states with real orbitals.

The HF energy is the expectation value of the true Hamiltonian with respect to the HF state:

$$E = \langle \mathrm{HF} | \, \hat{H} \, | \mathrm{HF} \rangle \, . \tag{2.17}$$

In second quantization, the Hamiltonian in the MO basis is given by

$$\hat{H} = \sum_{pq} h_{pq}^{\mathrm{mo}} E_{pq} + \frac{1}{2} \sum_{pqrs} g_{pqrs}^{\mathrm{mo}} e_{pqrs} + h_{\mathrm{nuc}}, \tag{2.18}$$

where E_{pq} and e_{pqrs} are the one- and two-electron excitation operators, respectively. The one- and two-electron integrals in atomic units are

$$h_{pq}^{\mathrm{mo}} = \int \phi_p^*(\mathbf{r}) \left(\frac{1}{2} \nabla^2 - \sum_I \frac{Z_I}{r_I} \right) \phi_q(\mathbf{r}) \mathrm{d}\mathbf{r} \tag{2.19}$$

and

$$g_{pqrs}^{\mathrm{mo}} = (pq|rs) = \iint \phi_p^*(\mathbf{r}_1) \phi_r^*(\mathbf{r}_2) \frac{1}{\mathbf{r}_{12}} \phi_q(\mathbf{r}_1) \phi_s(\mathbf{r}_2) \mathrm{d}\mathbf{r}_1 \mathrm{d}\mathbf{r}_2. \tag{2.20}$$

In the density formulation of HF, the energy is given by

$$E = 2 \sum_{pq} D_{pq}^{\mathrm{mo}} h_{pq}^{\mathrm{mo}} + \sum_{pqrs} d_{pqrs}^{\mathrm{mo}} g_{pqrs}^{\mathrm{mo}} + h_{\mathrm{nuc}}, \tag{2.21}$$

where the one- and two-electron densities are introduced. These are defined as

$$\begin{aligned} D_{pq}^{\mathrm{mo}} &= \frac{1}{2} \langle \mathrm{HF} | \, E_{pq} \, | \mathrm{HF} \rangle \\ d_{pqrs}^{\mathrm{mo}} &= \frac{1}{2} \langle \mathrm{HF} | \, e_{pqrs} \, | \mathrm{HF} \rangle \, , \end{aligned} \tag{2.22}$$

In an orthogonal MO basis, the condition

$$\mathbf{C}^{\mathrm{T}} \mathbf{S} \mathbf{C} = \mathbf{I} \tag{2.23}$$

holds and the one-electron density matrix has the diagonal structure shown in equation 2.9. For a closed-shell HF-state, the two-electron density may be written in terms of one-electron densities[3]. This, together with orthogonality, allows the HF energy to be written as

$$E = 2\mathrm{Tr}[\mathbf{D}^{\mathrm{mo}} \mathbf{h}^{\mathrm{mo}}] + \mathrm{Tr}[\mathbf{D}^{\mathrm{mo}} \mathbf{G}^{\mathrm{mo}}(\mathbf{D}^{\mathrm{mo}})] + h_{\mathrm{nuc}}, \tag{2.24}$$

where we have defined the matrix

$$G_{pq}^{\mathrm{mo}}(\mathbf{D}^{\mathrm{mo}}) = \sum_{rs} \left(2 g_{pqrs}^{\mathrm{mo}} - g_{psrq}^{\mathrm{mo}} \right) D_{rs}^{\mathrm{mo}}. \tag{2.25}$$

The density-based energy minimization is commonly carried out in the AO basis, in which the AO density matrix

$$\mathbf{D} = \mathbf{C} \mathbf{D}^{\mathrm{mo}} \mathbf{C}^{\mathrm{T}} \tag{2.26}$$

is introduced into the HF energy expression. By defining the transformation of the matrix elements as

$$\begin{aligned}\mathbf{h}^{\mathrm{mo}} &= \mathbf{C}^{\mathrm{T}}\mathbf{h}\mathbf{C} \\ \mathbf{G}^{\mathrm{mo}}(\mathbf{D}^{\mathrm{mo}}) &= \mathbf{C}^{\mathrm{T}}\mathbf{G}(\mathbf{D})\mathbf{C}\end{aligned} \tag{2.27}$$

and exploiting the cyclic permutation feature of the trace, we get the HF energy in the AO basis:

$$E = 2\mathrm{Tr}[\mathbf{D}\mathbf{h}] + \mathrm{Tr}[\mathbf{D}\mathbf{G}(\mathbf{D})] + h_{\mathrm{nuc}}. \tag{2.28}$$

The symmetry and trace conditions of the MO density (equation 2.1) translate to the AO density:

$$\mathbf{D}^{\mathrm{T}} = \mathbf{D}, \tag{2.29}$$

$$\mathrm{Tr}[\mathbf{D}\mathbf{S}] = \mathrm{Tr}[\mathbf{D}^{\mathrm{mo}}] = \frac{1}{2}N_{\mathrm{e}}. \tag{2.30}$$

Furthermore, the orthonormality of the MO space (equation 2.23) implies that the AO density matrix must satisfy the idempotency condition

$$(\mathbf{D}\mathbf{S})^2 = \mathbf{C}\mathbf{D}^{\mathrm{mo}}\mathbf{C}^{\mathrm{T}}\mathbf{S}\mathbf{C}\mathbf{D}^{\mathrm{mo}}\mathbf{C}^{\mathrm{T}}\mathbf{S} = \mathbf{D}\mathbf{S} \tag{2.31}$$

The minimization of the energy is achieved through the exponential parametrization of the density, which preserves these conditions. The exponential parametrization is detailed in section 2.1 for the MO basis, and its AO basis analogue is obtained by applying the AO transformation to the parametrized MO density (equation 2.3) and using the orthonormality condition (equation 2.23) and the identity [37]

$$\mathbf{B}\exp(\mathbf{A})\mathbf{B}^{-1} = \exp(\mathbf{B}\mathbf{A}\mathbf{B}^{-1}). \tag{2.32}$$

Defining the AO transformed antisymmetric matrix

$$\mathbf{X} = \mathbf{C}\boldsymbol{\kappa}\mathbf{C}^{\mathrm{T}} \tag{2.33}$$

we get the exponential parametrization of the AO density as

$$\mathbf{D}(\mathbf{X}) = \exp(-\mathbf{X}\mathbf{S})\mathbf{D}\exp(\mathbf{S}\mathbf{X}). \tag{2.34}$$

This parametrization may be represented as an *asymmetric BCH expansion* [3]

$$\mathbf{D}(\mathbf{X}) = \mathbf{D} + [\mathbf{D}, \mathbf{X}]_{\mathbf{S}} + \frac{1}{2!}[[\mathbf{D}, \mathbf{X}]_{\mathbf{S}}, \mathbf{X}]_{\mathbf{S}} + \ldots, \tag{2.35}$$

where

$$[\mathbf{D}, \mathbf{X}]_{\mathbf{S}} = \mathbf{D}\mathbf{S}\mathbf{X} - \mathbf{X}\mathbf{S}\mathbf{D} \tag{2.36}$$

is the so-called S commutator. The matrix $\mathbf{X}$ must obey a projection relation similar to equation 2.16, with the AO projectors

$$\begin{aligned}\mathbf{P} &= \mathbf{D}\mathbf{S} \\ \mathbf{Q} &= \mathbf{I} - \mathbf{D}\mathbf{S},\end{aligned} \tag{2.37}$$

to avoid redundant rotations.

$\mathbf{X}$ may be written in terms of its independent parameters as

$$\mathbf{X} = \sum_{\mu>\nu} X_{\mu\nu}(\mathbf{E}_{\mu\nu} - \mathbf{E}_{\nu\mu}) = \sum_{\mu>\nu} X_{\mu\nu}\mathbf{E}^{-}_{\mu\nu} \tag{2.38}$$

where $\mathbf{E}_{\mu\nu}$ are the so-called elementary matrices[3]. To find the electronic gradient, we evaluate the differentiated energy in the point $\mathbf{X} = \mathbf{0}$. The energy can be expressed as a function of $\mathbf{X}$ by inserting the parametrized density (equation 2.35) into the energy (equation 2.28), yielding

$$\begin{aligned} E(\mathbf{X}) = 2\mathrm{Tr}[\mathbf{Dh}] + \mathrm{Tr}[\mathbf{DG}(\mathbf{D})] + 2\mathrm{Tr}[[\mathbf{D},\mathbf{X}]_{\mathbf{S}}\mathbf{F}] \\ + \mathrm{Tr}[[\mathbf{D},\mathbf{X}]_{\mathbf{S}}\mathbf{G}([\mathbf{D},\mathbf{X}]_{\mathbf{S}})] + \dots \end{aligned} \tag{2.39}$$

where

$$\mathbf{F} = \mathbf{h} + \mathbf{G}(\mathbf{D}) \tag{2.40}$$

is the *Fock matrix*. Differentiating with respect to $X_{\mu\nu}$ and evaluating at $\mathbf{X} = \mathbf{0}$ yields

$$E^{(1)}_{\mu\nu} = 2\mathrm{Tr}[[\mathbf{D},\mathbf{E}^{-}_{\mu\nu}]_{\mathbf{S}}\mathbf{F}] = 2\mathrm{Tr}[\mathbf{E}^{-}_{\mu\nu}(\mathbf{FDS} - \mathbf{SDF})]. \tag{2.41}$$

Thus the convergence criteria for the energy optimization is

$$\mathbf{FDS} = \mathbf{SDF}. \tag{2.42}$$

For the actual optimization algorithm of the energy, there are a couple of options. One is the *density-based SCF method*, in which the Roothan-Hall equations are reformulated as a set of linear equations whose solution produces a new density matrix[3]. These equations are solved until the generated density equals the previous density. In contrast to the classical orbital-based SCF method, this method does not require the diagonalization of the Fock matrix, only the addition and multiplication of AO matrices, and linear scaling can be achieved[3].

Another option is to directly minimize the energy (equation 2.28) with respect to the density using one of the standard first- or second-order methods like the conjugate gradient or Newtons method. With Newtons method, we iteratively search for the minimum of a quadratic approximation to the energy function by solving the Newton equations

$$\mathbf{E}^{(2)}_n \Delta\mathbf{X}_n = -\mathbf{E}^{(1)}_n, \tag{2.43}$$

where $\mathbf{E}^{(1)}_n$ and $\mathbf{E}^{(2)}_n$ are the electronic gradient and Hessian of the n'th iteration, respectively, and $\mathbf{X}_n$ is the change in the variational parameters[3]. However, to directly solve the Newton equations would require the expensive inversion of the Hessian, and it is thus more economical to solve the equations in an iterative fashion. This is done by carrying out linear transformations of the Hessian on trial vectors $\mathbf{z}$:

$$\sigma = \mathbf{E}^{(2)}\mathbf{z}. \tag{2.44}$$

In the density formulation, this can be done in a way that avoids the explicit construction and storage of the Hessian[3].

2.3 Density based multilevel Hartree-Fock

This section will present the main points of the energy minimization in the density-based multilevel Hartree-Fock (MLHF) method in the MO basis as formulated by Sæther *et al.*[27]. Their derivation follows similar steps as the classical density HF approach described in section 2.2, but exploits the MO basis formulation to obtain a significant reduction in the dimensions of the matrices. The process yields a single MLHF wave function for the entire molecular system, thus introducing no breaking of bonds or other troublesome behaviour at the boundary between the active and inactive region.

In the MLHF approach, the density matrix is partitioned into an active and an inactive part,

$$\mathbf{D} = \mathbf{D}_\mathrm{a} + \mathbf{D}_\mathrm{e}, \tag{2.45}$$

each density representing a corresponding orbital space. We want these to be orthonormal spaces and thus require that each density fulfills the symmetry, trace, and idempotency conditions (equations 2.29, 2.30, 2.31). Their sum, in other words the total density, should also fulfill these conditions, implying not only the orthonormality of the total space, but also that the active and inactive spaces are orthogonal to each other. The goal of the method is to optimize just the active part, while the inactive part is modeled with a starting guess wave function which is never optimized. This can be accomplished by first generating a starting guess density for the whole system, which is then partitioned according to equation 2.45 by Cholesky decomposition as described by Myhre *et al.*[25]. Since the inactive density is never optimized, a reasonable starting guess should be chosen. One possibility is the superposition of atomic densities (SAD) starting guess by van Lenthe *et al.*[38].

The MLHF formulation allows for a reduction in dimensions of the active MO space, thus making it highly desirable to carry out the energy minimization in the MO basis. This reduction is performed as

$$\begin{aligned}
&\qquad\quad o_a \quad o_e \quad v_a \quad v_e \\
\mathbf{D}_\mathrm{a}^\mathrm{mo} = \; & \begin{matrix} o_a \\ o_e \\ v_a \\ v_e \end{matrix} \begin{pmatrix} \mathbf{1} & \mathbf{0} & \mathbf{0} & \mathbf{0} \\ \mathbf{0} & \mathbf{0} & \mathbf{0} & \mathbf{0} \\ \mathbf{0} & \mathbf{0} & \mathbf{0} & \mathbf{0} \\ \mathbf{0} & \mathbf{0} & \mathbf{0} & \mathbf{0} \end{pmatrix} \\
&\downarrow \\
&\qquad\quad o_a \quad v_a \\
\mathbf{D}_\mathrm{a,r}^\mathrm{mo} = \; & \begin{matrix} o_a \\ v_a \end{matrix} \begin{pmatrix} \mathbf{1} & \mathbf{0} \\ \mathbf{0} & \mathbf{0} \end{pmatrix},
\end{aligned} \tag{2.46}$$

from $N_\mathrm{ao} \times N_\mathrm{ao}$ to $N_\mathrm{ao}^\mathrm{a} \times N_\mathrm{ao}^\mathrm{a}$, where N_ao is the total number of AOs and N_ao^a is the number of active AOs. This is owing to the structure of the active MO density, which only has non-zero elements in the active occupied-active occupied block. The active MOs are generated from the starting guess SAD density, while the inactive MOs are never generated or referenced. This only needs to be performed once at the beginning of the procedure.

Inserting the partitioned MO density into the energy (equation 2.24) and applying the reduction of dimensions yields

$$\begin{aligned} E = &2\mathrm{Tr}[\mathbf{D}^{\mathrm{mo}}_{\mathrm{a,r}}\mathbf{h}^{\mathrm{mo}}_{\mathrm{r}}] + \mathrm{Tr}[\mathbf{D}^{\mathrm{mo}}_{\mathrm{a,r}}\mathbf{G}^{\mathrm{mo}}_{\mathrm{r}}(\mathbf{D}^{\mathrm{mo}}_{\mathrm{a,r}})] \\ &+ 2\mathrm{Tr}[\mathbf{D}^{\mathrm{mo}}_{\mathrm{e}}\mathbf{h}^{\mathrm{mo}}] + \mathrm{Tr}[\mathbf{D}^{\mathrm{mo}}_{\mathrm{e}}\mathbf{G}^{\mathrm{mo}}(\mathbf{D}^{\mathrm{mo}}_{\mathrm{e}})] \\ &+ 2\mathrm{Tr}[\mathbf{D}^{\mathrm{mo}}_{\mathrm{a,r}}\mathbf{G}^{\mathrm{mo}}_{\mathrm{r}}(\mathbf{D}^{\mathrm{mo}}_{\mathrm{e}})] + h_{\mathrm{nuc}}, \end{aligned} \tag{2.47}$$

where the subscript r denotes a matrix of reduced dimension. We have used the identity

$$\mathrm{Tr}[\mathbf{A}\mathbf{G}^{\mathrm{mo}}(\mathbf{B})] = \mathrm{Tr}[\mathbf{B}\mathbf{G}^{\mathrm{mo}}(\mathbf{A})], \tag{2.48}$$

which follows from the permutational symmetries of the two-electron integrals (equation 2.20) for real orbitals.

Equation 2.47 may be written in terms of the separate contributions from the active and inactive spaces:

$$E = e(\mathbf{D}^{\mathrm{mo}}_{\mathrm{a,r}}) + e(\mathbf{D}^{\mathrm{mo}}_{\mathrm{e}}) + 2\mathrm{Tr}[\mathbf{D}^{\mathrm{mo}}_{\mathrm{a,r}}\mathbf{G}^{\mathrm{mo}}_{\mathrm{r}}(\mathbf{D}^{\mathrm{mo}}_{\mathrm{e}})] + h_{\mathrm{nuc}}, \tag{2.49}$$

where

$$e(\mathbf{D}^{\mathrm{mo}}_{i}) = 2\mathrm{Tr}[\mathbf{D}^{\mathrm{mo}}_{i}\mathbf{h}^{\mathrm{mo}}] + \mathrm{Tr}[\mathbf{D}^{\mathrm{mo}}_{i}\mathbf{G}^{\mathrm{mo}}(\mathbf{D}^{\mathrm{mo}}_{i})]. \tag{2.50}$$

The energy minimization is achieved through rotations among active occupied and active virtual orbitals only. In other words, the active density is optimized through the exponential parametrization

$$\mathbf{D}^{\mathrm{mo}}_{\mathrm{a,r}}(\boldsymbol{\kappa}_{\mathrm{r}}) = \exp(-\boldsymbol{\kappa}_{\mathrm{r}})\mathbf{D}^{\mathrm{mo}}_{\mathrm{a,r}}\exp(\boldsymbol{\kappa}_{\mathrm{r}}) \tag{2.51}$$

while the inactive density remains unchanged throughout the minimization. To avoid redundant rotations, $\boldsymbol{\kappa}_{\mathrm{r}}$ is projected as

$$\boldsymbol{\kappa}_{\mathrm{r}} = \mathbf{P}^{\mathrm{mo}}_{\mathrm{a,r}}\boldsymbol{\kappa}_{\mathrm{r}}\mathbf{Q}^{\mathrm{mo}}_{\mathrm{a,r}} + \mathbf{Q}^{\mathrm{mo}}_{\mathrm{a,r}}\boldsymbol{\kappa}_{\mathrm{r}}\mathbf{P}^{\mathrm{mo}}_{\mathrm{a,r}} \tag{2.52}$$

with the projectors

$$\begin{aligned} \mathbf{P}^{\mathrm{mo}}_{\mathrm{a,r}} &= \mathbf{D}^{\mathrm{mo}}_{\mathrm{a,r}} \\ \mathbf{Q}^{\mathrm{mo}}_{\mathrm{a,r}} &= \mathbf{I} - \mathbf{D}^{\mathrm{mo}}_{\mathrm{a,r}}. \end{aligned} \tag{2.53}$$

Inserting the BCH expansion of the parametrization into the energy expression yields

$$\begin{aligned} E(\boldsymbol{\kappa}_{\mathrm{r}}) = &e(\mathbf{D}^{\mathrm{mo}}_{\mathrm{e}}) + 2\mathrm{Tr}[\mathbf{D}^{\mathrm{mo}}_{\mathrm{a,r}}\mathbf{h}^{\mathrm{mo}}_{\mathrm{r}}] + \mathrm{Tr}[\mathbf{D}^{\mathrm{mo}}_{\mathrm{a,r}}\mathbf{G}^{\mathrm{mo}}_{\mathrm{r}}(\mathbf{D}^{\mathrm{mo}}_{\mathrm{a,r}})] \\ &+ 2\mathrm{Tr}[\mathbf{D}^{\mathrm{mo}}_{\mathrm{a,r}}\mathbf{G}^{\mathrm{mo}}_{\mathrm{r}}(\mathbf{D}^{\mathrm{mo}}_{\mathrm{e}})] + \mathrm{Tr}[[\mathbf{D}^{\mathrm{mo}}_{\mathrm{a,r}}, \boldsymbol{\kappa}_{\mathrm{r}}]\mathbf{F}^{\mathrm{mo}}_{\mathrm{eff,r}}] + \ldots \end{aligned} \tag{2.54}$$

where we have defined the *effective Fock matrix*

$$\mathbf{F}^{\mathrm{mo}}_{\mathrm{eff,r}} = \mathbf{h}^{\mathrm{mo}}_{\mathrm{r}} + \mathbf{G}^{\mathrm{mo}}_{\mathrm{r}}(\mathbf{D}^{\mathrm{mo}}_{\mathrm{a,r}}) + \mathbf{G}^{\mathrm{mo}}_{\mathrm{r}}(\mathbf{D}^{\mathrm{mo}}_{\mathrm{e}}). \tag{2.55}$$

From here, the derivation of the electronic gradient is analogous to the full space HF method. Differentiating with respect to the independent elements of $\boldsymbol{\kappa}_{\mathrm{r}}$ and evaluating at $\boldsymbol{\kappa}_{\mathrm{r}} = \mathbf{0}$, we get

$$E^{(1)}_{pq} = 2\mathrm{Tr}[[\mathbf{D}^{\mathrm{mo}}_{\mathrm{a,r}}, \mathbf{E}^{-}_{pq,\mathrm{r}}]\mathbf{F}^{\mathrm{mo}}_{\mathrm{eff,r}}] = 2\mathrm{Tr}[\mathbf{E}^{-}_{pq,\mathrm{r}}(\mathbf{F}^{\mathrm{mo}}_{\mathrm{eff,r}}\mathbf{D}^{\mathrm{mo}}_{\mathrm{a,r}} - \mathbf{D}^{\mathrm{mo}}_{\mathrm{a,r}}\mathbf{F}^{\mathrm{mo}}_{\mathrm{eff,r}})]. \tag{2.56}$$

Thus the convergence criteria is

$$\mathbf{F}^{\mathrm{mo}}_{\mathrm{eff,r}}\mathbf{D}^{\mathrm{mo}}_{\mathrm{a,r}} = \mathbf{D}^{\mathrm{mo}}_{\mathrm{a,r}}\mathbf{F}^{\mathrm{mo}}_{\mathrm{eff,r}} \tag{2.57}$$

or equivalently

$$\mathbf{F}^{\mathrm{mo}}_{\mathrm{eff,r,vo}} = \mathbf{F}^{\mathrm{mo}}_{\mathrm{eff,r,ov}}. \tag{2.58}$$

The linear transformations of the electronic Hessian on a trial vector $\boldsymbol{\kappa}$ is

$$\begin{aligned}\mathbf{E}^{(2)}\boldsymbol{\kappa} = (\mathbf{F}^{\mathrm{mo}}_{\mathrm{eff,r,oo}} - \mathbf{F}^{\mathrm{mo}}_{\mathrm{eff,r,vv}})\boldsymbol{\kappa} + \boldsymbol{\kappa}(\mathbf{F}^{\mathrm{mo}}_{\mathrm{eff,r,vv}} - \mathbf{F}^{\mathrm{mo}}_{\mathrm{eff,r,oo}}) \\ - \mathbf{G}^{\mathrm{mo}}_{\mathrm{r,ov}}([\mathbf{D}^{\mathrm{mo}}_{\mathrm{a,r}}, \boldsymbol{\kappa}_{\mathrm{r}}]) + \mathbf{G}^{\mathrm{mo}}_{\mathrm{r,vo}}([\mathbf{D}^{\mathrm{mo}}_{\mathrm{a,r}}, \boldsymbol{\kappa}_{\mathrm{r}}]).\end{aligned} \tag{2.59}$$

The MLHF energy can now be minimized with an algorithm like the density-based SCF method or Newtons method as discussed for the full-space HF method in section 2.2. Sæther *et al.*[27] demonstrated the MLHF energy optimization using a Roothan-Hall (RH) quasi-Newton minimization, where the two-electron integral matrix terms of the electronic Hessian linear transformations (equation 2.59) are left out. Later, Høyvik[39] achieved accelerated convergence of the MLHF method through two different approaches: Combination of the RH process with the direct inversion in the iterative subspace (DIIS) method by Pulay[35], and the augmented RH method by Høst *et al.*[40].

2.4 Orbital connections

Now that the procedure for the MLHF energy minimization has been established, we can move on to consider geometrical perturbations of the molecular system. As it turns out, the change in molecular geometry upon an iterative step carries some substantial implications on how we expand our wave function in a basis set. Specifically, since our finite basis consists of AOs that are fixed on the nuclei, it will change in response to the geometry perturbation. This is an example of a so-called *perturbation-dependent basis set* (PDBS). Since there exist an infinite number of orthonormal sets of orbitals at each molecular geometry, the need arises for a method to unambiguously select exactly one of these sets at the next geometry. These methods of creating a one-to-one correspondence between orthonormal orbital sets at different perturbation strengths are known as *orbital connections*. Something worth noting is that this complication of having to select a different basis at each geometry arises because we are using a finite, incomplete basis[41]. This section will present some of the fundamental theory on orbital connections. For more details, see Olsen *et al.*[42].

Let the orthonormal molecular orbitals (OMOs) be given by

$$\psi_m(\mathrm{x}) = \sum_{\mu} \chi_\mu(\mathrm{x})C_{\mu m}(\mathrm{x}), \tag{2.60}$$

where χ_μ is the set of basis functions and x is a vector of external parameters, for instance the geometrical coordinates. The OMOs will in general differ from the final MOs after optimization has been carried out, but will be required to equal the optimized MOs for zero perturbation given by

$$\phi_m(\mathrm{x}_0) = \sum_\mu \chi_\mu(\mathrm{x}_0) C^{(0)}_{\mu m}. \tag{2.61}$$

These may be considered part of the unmodified MOs (UMOs) defined as

$$\phi_m(\mathrm{x}) = \sum_\mu \chi_\mu(\mathrm{x}) C^{(0)}_{\mu m}. \tag{2.62}$$

The UMOs are in general not orthogonal. The OMOs can now be written as

$$\psi_m(\mathrm{x}) = \sum_n \phi_n(\mathrm{x}) \mathbf{T}_{\mathrm{nm}}, \tag{2.63}$$

where the so-called *connection matrix* $\mathbf{T}$ fulfills

$$\begin{aligned} &\mathbf{T}^\dagger(\mathrm{x})\mathbf{S}(\mathrm{x})\mathbf{T}(\mathrm{x}) = 1 \\ &\mathbf{T}(\mathrm{x}_0) = 1. \end{aligned} \tag{2.64}$$

The latter requirement implies that the OMOs equal the UMOs at x_0. Equation 2.63 holds as long as the UMO overlap matrix $\mathbf{S}(\mathrm{x})$ is non-singular[42]. By rewriting

$$\mathbf{T}^\dagger(\mathrm{x})\mathbf{S}(\mathrm{x})\mathbf{T}(\mathrm{x}) = (\mathbf{S}^{\frac{1}{2}}\mathbf{T})^\dagger(\mathbf{S}^{\frac{1}{2}}\mathbf{T}) = 1 \tag{2.65}$$

we see that $\mathbf{S}^{\frac{1}{2}}\mathbf{T}$ is a unitary matrix and therefore may be expressed as the exponential of an antihermitian matrix as discussed in section 2.1. For a real space this corresponds to the exponential of an antisymmetric matrix, determined by a set of $\frac{1}{2}n(n-1)$ independent parameters as mentioned. Then by extension, the connection matrix T is uniquely determined by the same number of independent parameters. The choice of these parameters is what constitutes a particular orbital connection.

Some connections like the *Gram-Schmidt connection* and the *symmetric connection* are simple to set up, but lack any real physical significance. In contrast, if the *natural connection* introduced by Olsen *et al.*[42] is used, the calculation of molecular response properties is made more transparent in the sense that the equations reduce to terms which have meaningful relations to physical quantities. An example is the paramagnetic and diamagnetic terms in the calculation of magnetizabilities. This connection is set up so that the change in the OMOs upon perturbation is as small as possible.

As we shall see when deriving the MLHF molecular gradient (section 3.1), orbital connections in the density formalism correspond to establishing connections between the reference density matrices at different geometries, which will directly influence the MLHF molecular gradient expression.

2.5 The BFGS algorithm

The optimization of equilibrium geometries corresponds to locating a local minimum of the PES. This section presents some theory on the popular *Broyden-Fletcher-Goldfarb-Shanno* (BFGS) method which will be used in the iterative search for the minimum.

The BFGS method has its origin in Newtons method, a second order iterative method which approximates the PES by a quadratic surface within a local region. The i'th step towards the local PES minimum is given by the Newton equations:

$$\mathbf{s}_i = \mathbf{x}_i - \mathbf{x}_{i-1} = -\mathbf{H}_i^{-1}\mathbf{g}_i, \tag{2.66}$$

where $\mathbf{g}$ is the molecular gradient and $\mathbf{H}$ is the molecular Hessian. The step is defined as the difference between the new and old geometry. Solving the Newton equations involves the computationally expensive calculation and inversion of the Hessian matrix. An alternative is to use less expensive, approximate Hessians. In quasi-Newton methods an initial starting guess Hessian is used, and is updated in some manner in the subsequent iterations to produce approximate Hessians. The BFGS method is one such method, and uses the following update scheme for the approximate Hessian[33]:

$$\mathbf{G}_i^{\mathrm{BFGS}} = \mathbf{G}_{i-1} + \frac{\Delta\mathbf{g}_i \Delta\mathbf{g}_i^{\mathrm{T}}}{\Delta\mathbf{g}_i^{\mathrm{T}}\mathbf{s}_i} - \frac{\mathbf{G}_{i-1}\mathbf{s}_i\mathbf{s}_i^{\mathrm{T}}\mathbf{G}_{i-1}}{\mathbf{s}_i^{\mathrm{T}}\mathbf{G}_{i-1}\mathbf{s}_i}, \tag{2.67}$$

where $\mathbf{G}$ is the approximate Hessian and $\Delta\mathbf{g}_i = \mathbf{g}_i - \mathbf{g}_{i-1}$ is the gradient difference. The BFGS Hessian is well suited for minimizations since it is guaranteed to be positive definite as long as $\mathbf{G}_{k-1}$ is positive definite[33]. For more information on BFGS and other search methods, see Schlegel[1].

The quasi-Newton methods can also be reformulated to instead update the inverse Hessian directly and thus avoid the inversion step[1].

Approximate Hessian updating methods do not provide an initial Hessian for the optimization. The initial Hessian must instead be obtained in some other fashion. One obvious possibility is to calculate it exactly, although this might not always be possible. It may also be estimated in some fashion, for instance by empirical quantities, or by a Hessian calculation with MM or a lower level QM method. A crude approach is to simply use a scaled identity matrix as the initial Hessian[1]. Various model initial Hessians exist, an example of which was developed by Lindh *et al.*[43]. Bakken and Helgaker[33] achieved good performance with this model Hessian in combination with redundant internal coordinates.

2.6 The rational function method

An alternative to Newtons method is the related *Rational Function* (RF) method, where the local quadratic approximation to the surface is replaced by a local rational function approximation. Minimizing this rational function leads to the eigenvalue equation

$$\begin{pmatrix} \mathbf{H}_i & \mathbf{g}_i \\ \mathbf{g}_i^{\mathrm{T}} & 0 \end{pmatrix} \begin{pmatrix} \mathbf{s}_i \\ 1 \end{pmatrix} = \lambda_i \begin{pmatrix} \mathbf{s}_i \\ 1 \end{pmatrix}, \tag{2.68}$$

where left-hand side matrix is referred to as the *augmented Hessian*. This eigenvalue problem actually represents a system of equations

$$\begin{aligned} \mathbf{s}_i &= -(\mathbf{H}_i - \lambda_i \mathbf{I})^{-1} \mathbf{g}_i \\ \lambda_i &= \mathbf{g}_i^{\mathrm{T}} \mathbf{s}_i \end{aligned} \tag{2.69}$$

where the former is a level-shifted version of the Newton equation (equation 2.66). Solving equation 2.68 gives a particular eigenvector which, after scaling it so that its last element equals 1, contains the geometry step. When looking for a minimum, we chose the eigenvector associated with the smallest eigenvalue λ_i [44]. The Hessian used in the RF equation may be an approximate one provided by an updating scheme such as the BFGS Hessian (equation 2.67).

2.7 Step control

The convergence of Newtons method or the RF method is not guaranteed, as the quadratic surface or rational function approximations are only accurate within a local region around the reference point. If the Hessian has small eigenvalues, the produced step may become too large and overshoot the minimum, resulting in slow convergence or even no convergence altogether if the steps get stuck in a loop [1]. The step size may be restricted to avoid this in a number of ways. A simple approach is to set a hard threshold for the norm of the step, or for each step component. A better approach is to update this threshold in each iteration based on the accuracy of the quadratic surface or rational function at the previous geometry [33]. Another type of step control called a line search will only accept the step if it satisfies the Wolfe condition

$$\begin{aligned} \Delta E &< \alpha \mathbf{g}_i^{\mathrm{T}} \Delta \mathbf{x} \\ \mathbf{g}_{i+1}^{\mathrm{T}} \Delta \mathbf{x} &> \beta \mathbf{g}_i^{\mathrm{T}} \Delta \mathbf{x}, \end{aligned} \tag{2.70}$$

where $\mathbf{g}_i$ and $\mathbf{g}_{i+1}$ are the gradients in the current and new points, respectively, and α and β are chosen parameters between zero and one. If the Wolfe condition is not satisfied, the trial step is scaled down by some chosen factor to produce the next trial step. A disadvantage of this is that each trial step requires a separate energy and gradient calculation, an expensive approach especially for *ab initio* optimization. An alternative is to produce a step that satisfies the Wolfe conditions based on a polynomial fitting to the energy and gradient [1].

2.8 Coordinate systems

The choice of coordinates for the molecular geometry can have a great impact on the performance of geometry optimization methods. A poor choice of coordinates may compromise the quality of the optimization by having traits such as:

- Large variation in the stiffness of coordinates
- Strong coupling between the coordinates
- Large anharmonicity of the PES

Large variations in coordinate stiffness corresponds to an ill-conditioned Hessian matrix, in which the eigenvalues differ strongly in magnitude[1]. Strong coupling corresponds to large off-diagonal elements of the Hessian[1]. Both of these can slow down the optimization. Lastly the anharmonicity of the PES, if significant around the search area, means that the quadratic approximation of our method is poor, and the calculated step may be inaccurate.

The Cartesian coordinate system is perhaps the most used and well-known coordinate system, as it is simple and straightforward to implement. Unfortunately, these coordinates are strongly coupled when representing molecular systems. They are also redundant, as there are more such coordinates than the number of internal degrees of freedom in a molecular system. Certain transformations of such redundant coordinates will simply result in translation or rotation of the entire molecular system in space. There exist various internal coordinate systems which generally perform better than the Cartesian coordinates for geometry optimizations[33,45]. These consist of coordinates corresponding to molecular degrees of freedom such as bond lengths, bond angles, and dihedral angles, and can be either redundant or non-redundant. The Z-matrix internal coordinates are non-redundant, but may encounter problems especially for large or cyclical systems[33,46]. Various redundant and non-redundant internal coordinate systems have since been introduces, such as the redundant internal coordinates by Peng *et al.*[47], The *natural internal coordinates* by Pulay *et al.*[48] have the interesting property of minimizing the coupling between the coordinates.[44].

2.9 Hartree-Fock equilibrium geometries

The calculation of equilibrium geometries with HF is performed routinely in the literature[49–52]. This section will present some known aspects of the performance of HF in such calculations.

Equilibrium geometries obtained with HF usually differ from the exact equilibrium geometries by only a couple of picometers[3]. Bond angles usually differ by a couple of degrees[35,50]. Because HF lacks electron correlation energy, the electron-electron repulsion is underestimated, with the result that HF often gives bond lengths that are too short[53]. This effect is especially prominent for double bonds, triple bonds, and bonds containing highly electronegative atoms[50]. The inclusion of correlation energy by post-HF methods have in general been found to increase bond lengths[50,51]. Conversely, Helgaker *et al.*[51] found that improvements to the basis set tends to shorten bond lengths. They compared equilibrium geometries obtained with HF and various post-HF methods, for different-sized correlation consistent basis sets cc-pVDZ, cc-pVTZ, and cc-pVQZ. For certain combinations of correlation level and basis set size, a strong cancellation of errors occurred, resulting in highly accurate bond lengths. For HF, there was no gain in going beyond the cc-pVDZ basis set

since HF already undershoots the bond lengths; the only way to get improvements was to introduce correlation. Xie *et al.*[54] reached similar conclusions for correlation consistent basis sets with added polarization functions and f-like functions.

3 Molecular gradient in multilevel Hartree-Fock

3.1 Deriving the molecular gradient

This section will present in detail the derivation of the analytical MLHF molecular gradient in the AO basis which has been developed in this thesis. The approach is largely based on a derivation of the HF molecular gradient presented by Larsen *et al.*[55] and will mostly follow the same steps. Still, some subtleties will arise in the MLHF formulation.

The AO transformed MLHF energy (equation 2.47) is given by

$$\begin{aligned} E = &2\mathrm{Tr}[\mathbf{D}_\mathrm{a}\mathbf{h}] + \mathrm{Tr}[\mathbf{D}_\mathrm{a}\mathbf{G}(\mathbf{D}_\mathrm{a})] + 2\mathrm{Tr}[\mathbf{D}_\mathrm{e}\mathbf{h}] \\ &+ \mathrm{Tr}[\mathbf{D}_\mathrm{e}\mathbf{G}(\mathbf{D}_\mathrm{e})] + 2\mathrm{Tr}[\mathbf{D}_\mathrm{a}\mathbf{G}(\mathbf{D}_\mathrm{e})] + h_\mathrm{nuc}. \end{aligned} \tag{3.1}$$

By differentiating this energy with respect to a geometrical coordinate, we obtain an element of the molecular gradient. We will for simplicity use the shorthand notation

$$E^x \equiv \frac{\partial}{\partial k_q} E = [\mathbf{g}]_{kq} \tag{3.2}$$

to denote a general partial derivative with respect to a single spatial coordinate $q \in \{x, y, z\}$ of the k'th nucleus. In other words, this denotes a general element of the $3\times N_\mathrm{a}$ gradient matrix $\mathbf{g}$, where N_a is the number of atoms. For further simplicity, E^x will be referred to as just the "gradient" during the derivation.

Differentiating equation 3.1 yields

$$\begin{aligned} E^x = &2\mathrm{Tr}[(\mathbf{D}_\mathrm{a}^x + \mathbf{D}_\mathrm{e}^x)\mathbf{F}_\mathrm{eff}] + 2\mathrm{Tr}[\mathbf{D}_\mathrm{a}\mathbf{h}^x] + 2\mathrm{Tr}[\mathbf{D}_\mathrm{e}\mathbf{h}^x] \\ &+ \mathrm{Tr}[\mathbf{D}_\mathrm{a}\mathbf{G}^x(\mathbf{D}_\mathrm{a})] + \mathrm{Tr}[\mathbf{D}_\mathrm{e}\mathbf{G}^x(\mathbf{D}_\mathrm{e})] + 2\mathrm{Tr}[\mathbf{D}_\mathrm{a}\mathbf{G}^x(\mathbf{D}_\mathrm{e})] + h_\mathrm{nuc}^x. \end{aligned} \tag{3.3}$$

Here we have used the identity 2.48, and introduced the AO transformed effective Fock matrix (equation 2.55). Note the use of the following notation:

$$\mathrm{Tr}[\mathbf{A}\mathbf{G}^x(\mathbf{B})] = \sum_{ijkl} (2(ij|kl) - (il|kj))^x A_{ij} B_{kl}. \tag{3.4}$$

Because the AO basis is perturbation-dependent (see section 2.4), the AOs, and by extension the densities, will change throughout the geometry optimization. Even the inactive density $\mathbf{D}_\mathrm{e}$ will change, despite the fact that only active nuclei are perturbed, because it contains contributions from all AOs of the system. Consequently, its derivative $\mathbf{D}_\mathrm{e}^x$ must also be included. We cannot simply consider only the energy terms that depend on the active density, like we do in the energy minimization. For this reason we will for briefness write the gradient in terms of the total density as

$$E^x = 2\mathrm{Tr}[\mathbf{D}^x\mathbf{F}_\mathrm{eff}] + 2\mathrm{Tr}[\mathbf{D}\mathbf{h}^x] + \mathrm{Tr}[\mathbf{D}\mathbf{G}^x(\mathbf{D}_\mathrm{a})] + \mathrm{Tr}[\mathbf{D}\mathbf{G}^x(\mathbf{D}_\mathrm{e})] + h_\mathrm{nuc}^x \tag{3.5}$$

whenever specific reference to $\mathbf{D}_\mathrm{a}$ or $\mathbf{D}_\mathrm{e}$ is not necessary. We do however keep the differentiated two-electron integral matrix

$$\mathbf{G}^x(\mathbf{D}) = \mathbf{G}^x(\mathbf{D}_\mathrm{a}) + \mathbf{G}^x(\mathbf{D}_\mathrm{e}) \tag{3.6}$$

in separate terms for reasons explained later in this section.

The differentiated densities cannot be obtained explicitly and will therefore need to be expressed in terms of other quantities. To achieve this, we once again consider the exponential parametrization of the density expressed as an asymmetric BCH expansion (equation 2.35). Conditions on the $\mathbf{X}$ matrix can be inferred from the projection of its MO basis counterpart $\boldsymbol{\kappa}$ onto active occupied-active virtual space, which was carried out in the energy minimization (equation 2.52). Without reducing the dimensions of the MO space, the projection of $\boldsymbol{\kappa}$ uses the projectors $\mathbf{P}_\mathrm{a}^\mathrm{mo} = \mathbf{D}_\mathrm{a}^\mathrm{mo}$ and $\mathbf{Q}_\mathrm{a}^\mathrm{mo}$ given by

$$\mathbf{Q}_\mathrm{a}^\mathrm{mo} = \begin{array}{c} \\ o_a \\ o_e \\ v_a \\ v_e \end{array} \begin{array}{c} \begin{array}{cccc} o_a & o_e & v_a & v_e \end{array} \\ \begin{pmatrix} \mathbf{0} & \mathbf{0} & \mathbf{0} & \mathbf{0} \\ \mathbf{0} & \mathbf{0} & \mathbf{0} & \mathbf{0} \\ \mathbf{0} & \mathbf{0} & \mathbf{1} & \mathbf{0} \\ \mathbf{0} & \mathbf{0} & \mathbf{0} & \mathbf{0} \end{pmatrix} \end{array}. \tag{3.7}$$

By then using the orthonormality, we arrive at

$$\begin{aligned} \mathbf{X} &= \mathbf{C}\boldsymbol{\kappa}\mathbf{C}^\mathrm{T} = \mathbf{C}\mathbf{P}_\mathrm{a}^\mathrm{mo}\boldsymbol{\kappa}\mathbf{Q}_\mathrm{a}^\mathrm{mo}\mathbf{C}^\mathrm{T} + \mathbf{C}\mathbf{Q}_\mathrm{a}^\mathrm{mo}\boldsymbol{\kappa}\mathbf{P}_\mathrm{a}^\mathrm{mo}\mathbf{C}^\mathrm{T} \\ &= \mathbf{C}\mathbf{P}_\mathrm{a}^\mathrm{mo}\mathbf{C}^\mathrm{T}\mathbf{S}\mathbf{C}\boldsymbol{\kappa}\mathbf{C}^\mathrm{T}\mathbf{S}\mathbf{C}\mathbf{Q}_\mathrm{a}^\mathrm{mo}\mathbf{C}^\mathrm{T} + \mathbf{C}\mathbf{Q}_\mathrm{a}^\mathrm{mo}\mathbf{C}^\mathrm{T}\mathbf{S}\mathbf{C}\boldsymbol{\kappa}\mathbf{C}^\mathrm{T}\mathbf{S}\mathbf{C}\mathbf{P}_\mathrm{a}^\mathrm{mo}\mathbf{C}^\mathrm{T} \\ &= \mathbf{P}_\mathrm{a}\mathbf{X}\mathbf{Q}_\mathrm{a}^\mathrm{T} + \mathbf{Q}_\mathrm{a}\mathbf{X}\mathbf{P}_\mathrm{a}^\mathrm{T} \end{aligned} \tag{3.8}$$

where we have defined

$$\begin{aligned} \mathbf{P}_\mathrm{a} &= \mathbf{C}\mathbf{P}_\mathrm{a}^\mathrm{mo}\mathbf{C}^\mathrm{T}\mathbf{S} \\ \mathbf{Q}_\mathrm{a} &= \mathbf{C}\mathbf{Q}_\mathrm{a}^\mathrm{mo}\mathbf{C}^\mathrm{T}\mathbf{S} \end{aligned} \tag{3.9}$$

Furthermore, the structure and idempotency of the MO projectors implies that

$$\begin{aligned} \mathbf{P}_\mathrm{a} &= \mathbf{C}_\mathrm{oa}\mathbf{C}_\mathrm{oa}^\mathrm{T}\mathbf{S} = \mathbf{D}_\mathrm{a}\mathbf{S} \\ \mathbf{Q}_\mathrm{a} &= \mathbf{C}_\mathrm{va}\mathbf{C}_\mathrm{va}^\mathrm{T}\mathbf{S} \end{aligned} \tag{3.10}$$

where $\mathbf{C}_\mathrm{oa}$ contains the active occupied columns of the MO coefficient matrix $\mathbf{C}$ and zeros elsewhere, and similarly $\mathbf{C}_\mathrm{va}$ contains the active virtual columns of $\mathbf{C}$ and zeros elsewhere.

Expanding the S commutator of the BCH expansion (equation 2.35) and inserting the projection yields

$$[\mathbf{D}, \mathbf{X}]_\mathbf{S} = \mathbf{D}\mathbf{S}\mathbf{P}_\mathrm{a}\mathbf{X}\mathbf{Q}_\mathrm{a}^\mathrm{T} + \mathbf{D}\mathbf{S}\mathbf{Q}_\mathrm{a}\mathbf{X}\mathbf{P}_\mathrm{a}^\mathrm{T} - \mathbf{P}_\mathrm{a}\mathbf{X}\mathbf{Q}_\mathrm{a}^\mathrm{T}\mathbf{S}\mathbf{D} - \mathbf{Q}_\mathrm{a}\mathbf{X}\mathbf{P}_\mathrm{a}^\mathrm{T}\mathbf{S}\mathbf{D}. \tag{3.11}$$

Since $\mathbf{P}_\mathrm{a}$ projects onto active occupied space, it follows that

$$\begin{aligned}\mathbf{DSP}_\mathrm{a} &= \mathbf{D}_\mathrm{a}\mathbf{SP}_\mathrm{a} \\ \mathbf{P}_\mathrm{a}^\mathrm{T}\mathbf{SD} &= \mathbf{P}_\mathrm{a}^\mathrm{T}\mathbf{SD}_\mathrm{a},\end{aligned} \tag{3.12}$$

as the inactive density is projected onto zero. When projecting with $\mathbf{Q}_\mathrm{a}$ both the active and inactive densities are projected onto zero; however, keeping just the active term in the equation by writing

$$\begin{aligned}\mathbf{DSQ}_\mathrm{a} &= \mathbf{0} = \mathbf{D}_\mathrm{a}\mathbf{SQ}_\mathrm{a} \\ \mathbf{Q}_\mathrm{a}^\mathrm{T}\mathbf{SD} &= \mathbf{0} = \mathbf{Q}_\mathrm{a}^\mathrm{T}\mathbf{SD}_\mathrm{a}\end{aligned} \tag{3.13}$$

is helpful simply for the sake of the mathematical derivation. With these projections, the S commutator reduces to

$$[\mathbf{D}, \mathbf{X}]_\mathbf{S} = [\mathbf{D}_\mathrm{a}, \mathbf{X}]_\mathbf{S}. \tag{3.14}$$

Now we differentiate $\mathbf{D}(\mathbf{X})$, yielding

$$\mathbf{D}^x(\mathbf{X}) = \mathbf{D}^x + [\mathbf{D}_\mathrm{a}, \mathbf{X}]_\mathbf{S}^x + \frac{1}{2}[[\mathbf{D}_\mathrm{a}, \mathbf{X}]_\mathbf{S}, \mathbf{X}]_\mathbf{S}^x + ... \tag{3.15}$$

Evaluating at $\mathrm{x} = \mathrm{x}_0$ and $\mathbf{X} = \mathbf{0}$ will represent an expansion around the reference geometry. Every term except the first two will disappear since all terms of the nested commutators contain $\mathbf{X}$. The terms containing $\mathbf{X}$ in the differentiated commutator also vanish, leaving

$$\mathbf{D}^x(\mathbf{0}) = \mathbf{D}^x + [\mathbf{D}_\mathrm{a}, \mathbf{X}^x]_\mathbf{S}. \tag{3.16}$$

Although $\mathbf{D}(\mathbf{0}) = \mathbf{D}$, note that $\mathbf{D}^x(\mathbf{0}) \neq \mathbf{D}^x$. The latter is the differentiated reference density, while the former is the differentiated parametrized density evaluated in the point $\mathbf{X} = \mathbf{0}$.

Now we shall take a closer look at the differentiated reference density $\mathbf{D}^x$, and it becomes necessary to introduce two additional projectors

$$\begin{aligned}\mathbf{P}_\mathrm{e}^\mathrm{mo} &= \begin{array}{c} \\ o_a \\ o_e \\ v_a \\ v_e \end{array} \begin{array}{c} \begin{array}{cccc} o_a & o_e & v_a & v_e \end{array} \\ \begin{pmatrix} \mathbf{0} & \mathbf{0} & \mathbf{0} & \mathbf{0} \\ \mathbf{0} & \mathbf{1} & \mathbf{0} & \mathbf{0} \\ \mathbf{0} & \mathbf{0} & \mathbf{0} & \mathbf{0} \\ \mathbf{0} & \mathbf{0} & \mathbf{0} & \mathbf{0} \end{pmatrix} \end{array} \\ \mathbf{Q}_\mathrm{e}^\mathrm{mo} &= \begin{array}{c} \\ o_a \\ o_e \\ v_a \\ v_e \end{array} \begin{array}{c} \begin{array}{cccc} o_a & o_e & v_a & v_e \end{array} \\ \begin{pmatrix} \mathbf{0} & \mathbf{0} & \mathbf{0} & \mathbf{0} \\ \mathbf{0} & \mathbf{0} & \mathbf{0} & \mathbf{0} \\ \mathbf{0} & \mathbf{0} & \mathbf{0} & \mathbf{0} \\ \mathbf{0} & \mathbf{0} & \mathbf{0} & \mathbf{1} \end{pmatrix} \end{array},\end{aligned} \tag{3.17}$$

and their AO transformed counterparts

$$\begin{aligned}\mathbf{P}_\mathrm{e} &= \mathbf{C}\mathbf{P}_\mathrm{e}^\mathrm{mo}\mathbf{C}^\mathrm{T}\mathbf{S} = \mathbf{C}_\mathrm{oe}\mathbf{C}_\mathrm{oe}^\mathrm{T}\mathbf{S} = \mathbf{D}_\mathrm{e}\mathbf{S} \\ \mathbf{Q}_\mathrm{e} &= \mathbf{C}\mathbf{P}_\mathrm{e}^\mathrm{mo}\mathbf{C}^\mathrm{T}\mathbf{S} = \mathbf{C}_\mathrm{ve}\mathbf{C}_\mathrm{ve}^\mathrm{T}\mathbf{S}\end{aligned} \tag{3.18}$$

which project onto inactive occupied and inactive virtual space, respectively. The importance of this is to achieve the property

$$\mathbf{P}_\mathrm{a} + \mathbf{P}_\mathrm{e} + \mathbf{Q}_\mathrm{a} + \mathbf{Q}_\mathrm{e} = \mathbf{I}, \tag{3.19}$$

which allows us to separately consider all projections of the differentiated reference density through the identity

$$\mathbf{D}^x = (\mathbf{P}_\mathrm{a} + \mathbf{P}_\mathrm{e} + \mathbf{Q}_\mathrm{a} + \mathbf{Q}_\mathrm{e})\mathbf{D}^x(\mathbf{P}_\mathrm{a}^\mathrm{T} + \mathbf{P}_\mathrm{e}^\mathrm{T} + \mathbf{Q}_\mathrm{a}^\mathrm{T} + \mathbf{Q}_\mathrm{e}^\mathrm{T}). \tag{3.20}$$

Recall the idempotency of the reference density (equation 2.31), which must remain true through the geometry iterations if the reference density is to be valid. As it turns out, the idempotency will place certain constraints on the individual projections of $\mathbf{D}^x$, and this will allow us to obtain an expression for $\mathbf{D}^x$. The idempotency implies

$$\mathbf{D}^x = (\mathbf{DSD})^x = \mathbf{D}^x\mathbf{SD} + \mathbf{DS}^x\mathbf{D} + \mathbf{DSD}^x, \tag{3.21}$$

and so each term of equation 3.20 can be evaluated separately by inserting equation 3.21. For example:

$$\begin{aligned}\mathbf{P}_\mathrm{a}\mathbf{D}^x\mathbf{P}_\mathrm{a}^\mathrm{T} &= \mathbf{P}_\mathrm{a}\mathbf{D}^x\mathbf{SDP}_\mathrm{a}^\mathrm{T} + \mathbf{P}_\mathrm{a}\mathbf{DS}^x\mathbf{DP}_\mathrm{a}^\mathrm{T} + \mathbf{P}_\mathrm{a}\mathbf{DSD}^x\mathbf{P}_\mathrm{a}^\mathrm{T} \\ &= \mathbf{P}_\mathrm{a}\mathbf{D}^x\mathbf{P}_\mathrm{a}^\mathrm{T} + \mathbf{D}_\mathrm{a}\mathbf{SD}_\mathrm{a} + \mathbf{P}_\mathrm{a}\mathbf{D}^x\mathbf{P}_\mathrm{a}^\mathrm{T},\end{aligned} \tag{3.22}$$

where we have used the fact that $\mathbf{P}_\mathrm{a} = \mathbf{D}_\mathrm{a}\mathbf{S}$ and is idempotent. The other terms containing only $\mathbf{P}$'s are evaluated similarly, yielding

$$\begin{aligned}\mathbf{P}_\mathrm{a}\mathbf{D}^x\mathbf{P}_\mathrm{a}^\mathrm{T} &= -\mathbf{D}_\mathrm{a}\mathbf{S}^x\mathbf{D}_\mathrm{a} \\ \mathbf{P}_\mathrm{a}\mathbf{D}^x\mathbf{P}_\mathrm{e}^\mathrm{T} &= -\mathbf{D}_\mathrm{a}\mathbf{S}^x\mathbf{D}_\mathrm{e} \\ \mathbf{P}_\mathrm{e}\mathbf{D}^x\mathbf{P}_\mathrm{a}^\mathrm{T} &= -\mathbf{D}_\mathrm{e}\mathbf{S}^x\mathbf{D}_\mathrm{a} \\ \mathbf{P}_\mathrm{e}\mathbf{D}^x\mathbf{P}_\mathrm{e}^\mathrm{T} &= -\mathbf{D}_\mathrm{e}\mathbf{S}^x\mathbf{D}_\mathrm{e}.\end{aligned} \tag{3.23}$$

The terms containing only $\mathbf{Q}$'s are zero because these project densities onto zero. Lastly, the mixed terms, e.g.

$$\begin{aligned}\mathbf{P}_\mathrm{a}\mathbf{D}^x\mathbf{Q}_\mathrm{a}^\mathrm{T} &= \mathbf{P}_\mathrm{a}\mathbf{D}^x\mathbf{SDQ}_\mathrm{a}^\mathrm{T} + \mathbf{P}_\mathrm{a}\mathbf{DS}^x\mathbf{DQ}_\mathrm{a}^\mathrm{T} + \mathbf{P}_\mathrm{a}\mathbf{DSD}^x\mathbf{Q}_\mathrm{a}^\mathrm{T} \\ &= \mathbf{P}_\mathrm{a}\mathbf{DSD}^x\mathbf{Q}_\mathrm{a}^\mathrm{T} = \mathbf{P}_\mathrm{a}\mathbf{D}^x\mathbf{Q}_\mathrm{a}^\mathrm{T}\end{aligned} \tag{3.24}$$

are undetermined by the idempotency of the density, and we may therefore choose to set these terms to zero without affecting the validity of the density. Then in total, the differentiated reference density is given by

$$\mathbf{D}^x = -\mathbf{DS}^x\mathbf{D}. \tag{3.25}$$

It should be noted that setting the mixed projections of $\mathbf{D}^x$ to zero is a choice we make that establishes a particular connection between densities at different geometries, and that this connection is set up to preserve the idempotency of the density. In other words, we have established an orbital connection, ensuring that the orthogonality of the active, inactive, and total spaces is preserved upon perturbation. This particular choice of connection minimizes the norm of $\mathbf{D}^x$, and is conceptually similar to the natural connection of MO theory[55].

With this choice, the first term of the gradient (equation 3.5) becomes

$$\begin{aligned} 2\mathrm{Tr}[\mathbf{D}^x(\mathbf{0})\mathbf{F}_{\mathrm{eff}}] &= 2\mathrm{Tr}[\mathbf{D}^x\mathbf{F}_{\mathrm{eff}}] + 2\mathrm{Tr}[[\mathbf{D}_{\mathrm{a}}, \mathbf{X}^x]_{\mathbf{S}}\mathbf{F}_{\mathrm{eff}}] \\ &= -2\mathrm{Tr}[\mathbf{D}\mathbf{S}^x\mathbf{D}\mathbf{F}_{\mathrm{eff}}] + 2\mathrm{Tr}[\mathbf{X}^x(\mathbf{F}_{\mathrm{eff}}\mathbf{D}_{\mathrm{a}}\mathbf{S} - \mathbf{S}\mathbf{D}_{\mathrm{a}}\mathbf{F}_{\mathrm{eff}})] \end{aligned} \tag{3.26}$$

We recognize $\mathbf{F}_{\mathrm{eff}}\mathbf{D}_{\mathrm{a}}\mathbf{S} - \mathbf{S}\mathbf{D}_{\mathrm{a}}\mathbf{F}_{\mathrm{eff}}$ as the convergence criteria for the energy minimization. At the reference geometry the energy has been minimized, so this quantity is zero. This leaves us with the final expression for the MLHF molecular gradient:

$$E^x = 2\mathrm{Tr}[\mathbf{D}\mathbf{h}^x] + \mathrm{Tr}[\mathbf{D}\mathbf{G}^x(\mathbf{D}_{\mathrm{a}})] + \mathrm{Tr}[\mathbf{D}\mathbf{G}^x(\mathbf{D}_{\mathrm{e}})] - 2\mathrm{Tr}[\mathbf{D}\mathbf{S}^x\mathbf{D}\mathbf{F}_{\mathrm{eff}}] + h^x_{\mathrm{nuc}}. \tag{3.27}$$

This is actually exactly equivalent to the AO molecular gradient of full space HF given by Larsen *et al.*[55], as can be seen by substituting equation 3.6. Granted, the derivation in the MLHF formalism required a couple of detours. As pointed out by Larsen for the full space HF derivation, this density based formulation does not require the diagonalization of the (effective) Fock matrix in order to determine the perturbed density. The molecular gradient is given entirely in terms of the differentiated one- and two-electron integral matrices and the differentiated AO overlap matrix.

As discussed at the beginning of this section, equation 3.27 represents one element of the gradient matrix $\mathbf{g}$, corresponding to a partial derivative of the energy with respect to a single geometrical coordinate. The physical interpretation of these partial derivatives is that they are the negative of the forces acting on the nuclei. The convergence of the geometry towards an equilibrium can in this sense be viewed as a relaxation of these forces.

Since a MLHF geometry optimization aims to only optimize a small local region of the molecular system, the gradient elements corresponding to nuclei outside of this region should always be zero, thus enforcing these nuclei not to move. In the current work this was achieved by explicitly setting these gradient elements to zero in a procedure referred to as *frozen atoms* which will be detailed in the implementation (section 4.1). Ultimately, we expect that this effect of freezing the inactive region in space can be achieved directly through an active MO formulation where the gradient vanishes for inactive atoms, but such a formulation has not been worked out in this thesis. The idea of an MO driven geometry optimization is furthermore appealing if a reduction of dimensions similar to that of the energy minimization is possible.

An important note about the molecular gradient is that, since the one- and two-electron integral terms $\mathbf{h}$, $\mathbf{G}(\mathbf{D}_{\mathrm{a}})$, $\mathbf{G}(\mathbf{D}_{\mathrm{e}})$, as well as the overlap $\mathbf{S}$ are all matrices of dimensions $N_{ao} \times N_{ao}$ (N_{ao} being the number of AOs), each gradient element involves a distinct derivative of $N_{ao} \times N_{ao}$ matrices. It it therefore not hard to imagine that the calculation of these differentiated matrices will represent one of the more computationally expensive steps of the geometry optimization. This is especially true of the differentiated two-electron integral matrices. However, because of the locality of the active AO space, $\mathbf{D}_{\mathrm{a}}$ will be a sparse matrix, containing mostly zeros (or close-to-zero values) except for a localized section of the matrix. This should make it possible to design effective and cheap ways to construct $\mathbf{G}^x(\mathbf{D}_{\mathrm{a}})$. For this reason, we separate the differentiated two-electron integral matrix according to

equation 3.6. The $\mathbf{G}^x(\mathbf{D}_\mathrm{e})$ matrix is a different story, since the inactive density does not have this kind of sparsity. One way to lessen the computational cost would be to find some cheap way to calculate $\mathbf{G}^x(\mathbf{D}_\mathrm{e})$ exactly. Another is to find a cheap and reasonably accurate approximation. In this thesis, two such approximations have been tested, and are detailed in section 3.2.

3.2 Approximations of the differentiated two-electron integral matrix

In an attempt to tackle the time consuming step of constructing the differentiated two-electron integral matrix $\mathbf{G}^x(\mathbf{D}_\mathrm{e})$, two approximations to this matrix have been devised based on simple updating schemes. These will now be presented.

We may write the inactive density after a geometry perturbation as

$$\tilde{\mathbf{D}}_\mathrm{e} = \mathbf{D}_\mathrm{e} + \Delta\mathbf{D}_\mathrm{e}, \tag{3.28}$$

where $\tilde{\mathbf{D}}_\mathrm{e}$ is the inactive density after perturbation. In other words, the density of the current iteration equals the density of the previous iteration plus a small change. We can then write the differentiated two-electron integral matrix of the current iteration as

$$\tilde{\mathbf{G}}^x(\tilde{\mathbf{D}}_\mathrm{e}) = \tilde{\mathbf{G}}^x(\mathbf{D}_\mathrm{e}) + \tilde{\mathbf{G}}^x(\Delta\mathbf{D}_\mathrm{e}). \tag{3.29}$$

The important point is that $\Delta\mathbf{D}_\mathrm{e}$ is likely to be a sparse matrix since, out of the inactive AOs, the perturbation should only significantly affect those that are close to the active region. Thus the calculation of $\tilde{\mathbf{G}}^x(\Delta\mathbf{D}_\mathrm{e})$ should be cheap. By then making the approximation

$$\tilde{\mathbf{G}}^x(\tilde{\mathbf{D}}_\mathrm{e}) \approx \tilde{\mathbf{A}}^x(\tilde{\mathbf{D}}_\mathrm{e}) = \mathbf{A}^x(\mathbf{D}_\mathrm{e}) + \tilde{\mathbf{G}}^x(\Delta\mathbf{D}_\mathrm{e}), \tag{3.30}$$

where $\mathbf{A}^x(\mathbf{D}_\mathrm{e})$ is the approximate matrix of the previous iteration, we arrive at a cheap approximate updating scheme. This will hereafter be referred to as the A-approximation. In each iteration, the density $\tilde{\mathbf{D}}_\mathrm{e}$ and matrix $\tilde{\mathbf{A}}^x(\tilde{\mathbf{D}}_\mathrm{e})$ must be kept in memory or saved to a file for the next iteration. Note that in the first iteration, $\mathbf{D}_\mathrm{e} = 0$, $\mathbf{A}^x(\mathbf{D}_\mathrm{e}) = 0$, and $\tilde{\mathbf{A}}^x(\tilde{\mathbf{D}}_\mathrm{e}) = \tilde{\mathbf{G}}^x(\tilde{\mathbf{D}}_\mathrm{e})$, the exact matrix. The updating algorithm for the A-approximation is illustrated in Figure 4.12.

Let us take a closer look at what effects the A-approximation is neglecting. In the second iteration the exact matrix is given by the elements

$$\begin{aligned}
[\tilde{\mathbf{G}}^x(\tilde{\mathbf{D}}_\mathrm{e})]_{ij} &= \sum_{kl} \tilde{G}^x_{ijkl}[\tilde{\mathbf{D}}_\mathrm{e}]_{kl} \\
&= [\tilde{\mathbf{G}}^x(\mathbf{D}_\mathrm{e} + \Delta\mathbf{D}_\mathrm{e})]_{ij} = \sum_{kl} \tilde{G}^x_{ijkl}[\mathbf{D}_\mathrm{e}]_{kl} + \sum_{kl} \tilde{G}^x_{ijkl}[\Delta\mathbf{D}_\mathrm{e}]_{kl},
\end{aligned} \tag{3.31}$$

where we have used for simplicity the notation

$$G^x_{ijkl} = (2(ij|kl) - (il|kj))^x \tag{3.32}$$

for the differentiated two-electron integrals. The approximate matrix elements, on the other hand, are in the second iteration given by

$$[\tilde{\mathbf{A}}^x(\tilde{\mathbf{D}}_\mathrm{e})]_{ijkl} = \sum_{kl} G^x_{ijkl}[\mathbf{D}_\mathrm{e}]_{kl} + \sum_{kl} \tilde{G}^x_{ijkl}[\Delta\mathbf{D}_\mathrm{e}]_{kl} \qquad \text{(2nd iteration)}, \tag{3.33}$$

which neglects to update the differentiation of the two-electron integrals in the first sum to the current geometry. In a sense, we are assuming that the changes in two-electron interactions between two iterations is captured almost completely by the change in density $\Delta\mathbf{D}_\mathrm{e}$, and the interactions associated with the rest of the density are almost constant. If $\Delta\mathbf{D}_\mathrm{e}$ is sparse, we thereby only need to calculate relatively few of the differentiated integrals; only in the 1st iteration do we calculate all of them.

The second approximation, hereafter referred to as the B-approximation, is based on leaving out certain blocks of the inactive density in the exact calculation. Because the eT program reorders the list of atoms so that active atoms are at the top of the list, the AO inactive density matrix will have the following block structure:

$$\mathbf{D}_\mathrm{e} = \begin{pmatrix} \mathbf{aa} & \mathbf{ae} \\ \mathbf{ea} & \mathbf{ee} \end{pmatrix}, \tag{3.34}$$

i.e. containing an active-active, active-inactive, inactive-active, and inactive-inactive block. We will hereafter use the notations

$$\mathbf{D}_\mathrm{e}^\mathrm{aa} = \begin{pmatrix} \mathbf{aa} & \mathbf{0} \\ \mathbf{0} & \mathbf{0} \end{pmatrix} \tag{3.35}$$

and

$$\mathbf{D}_\mathrm{e}^\mathrm{u} = \begin{pmatrix} \mathbf{0} & \mathbf{ae} \\ \mathbf{ea} & \mathbf{ee} \end{pmatrix}, \tag{3.36}$$

with the relation

$$\mathbf{D}_\mathrm{e} = \mathbf{D}_\mathrm{e}^\mathrm{aa} + \mathbf{D}_\mathrm{e}^\mathrm{u}. \tag{3.37}$$

We may write the density after perturbation as

$$\tilde{\mathbf{D}}_\mathrm{e} = \tilde{\mathbf{D}}_\mathrm{e}^\mathrm{aa} + \mathbf{D}_\mathrm{e}^\mathrm{u} + \Delta\mathbf{D}_\mathrm{e}^\mathrm{u} \tag{3.38}$$

and further the differentiated two-electron integral matrix as

$$\begin{aligned} \tilde{\mathbf{G}}^x(\tilde{\mathbf{D}}_\mathrm{e}) &= \tilde{\mathbf{G}}^x(\tilde{\mathbf{D}}_\mathrm{e}^\mathrm{aa}) + \tilde{\mathbf{G}}^x(\tilde{\mathbf{D}}_\mathrm{e}^\mathrm{u}) \\ &= \tilde{\mathbf{G}}^x(\tilde{\mathbf{D}}_\mathrm{e}^\mathrm{aa}) + \tilde{\mathbf{G}}^x(\mathbf{D}_\mathrm{e}^\mathrm{u}) + \tilde{\mathbf{G}}^x(\Delta\mathbf{D}_\mathrm{e}^\mathrm{u}). \end{aligned} \tag{3.39}$$

The B-approximation approximates only part of the full matrix, namely

$$\tilde{\mathbf{G}}^x(\tilde{\mathbf{D}}_\mathrm{e}^\mathrm{u}) \approx \tilde{\mathbf{B}}^x(\tilde{\mathbf{D}}_\mathrm{e}^\mathrm{u}) = \mathbf{B}^x(\mathbf{D}_\mathrm{e}^\mathrm{u}) + \tilde{\mathbf{G}}^x(\Delta\mathbf{D}_\mathrm{e}^\mathrm{u}), \tag{3.40}$$

where $\mathbf{B}^x(\mathbf{D}_\mathrm{e}^\mathrm{u})$ is the approximate matrix of the previous iteration. In the first iteration, $\mathbf{B}^x(\mathbf{D}_\mathrm{e}^\mathrm{u}) = 0$ while $\tilde{\mathbf{B}}^x(\tilde{\mathbf{D}}_\mathrm{e}^\mathrm{u}) = \tilde{\mathbf{G}}^x(\tilde{\mathbf{D}}_\mathrm{e}^\mathrm{u})$, the exact u-part of the full matrix.

Inserting equation 3.40 into equation 3.39, we arrive at the approximation for the full matrix:

$$\tilde{\mathbf{G}}^x(\tilde{\mathbf{D}}_\mathrm{e}) \approx \tilde{\mathbf{B}}^x(\tilde{\mathbf{D}}_\mathrm{e}) = \tilde{\mathbf{G}}^x(\tilde{\mathbf{D}}_\mathrm{e}^{\mathrm{aa}}) + \tilde{\mathbf{B}}^x(\tilde{\mathbf{D}}_\mathrm{e}^{\mathrm{u}}). \tag{3.41}$$

In each iteration, the density $\tilde{\mathbf{D}}_\mathrm{e}^{\mathrm{u}}$ and matrix $\tilde{\mathbf{B}}^x(\tilde{\mathbf{D}}_\mathrm{e}^{\mathrm{u}})$ must be kept in memory or saved to a file for the next iteration. If the matrices $\tilde{\mathbf{D}}_\mathrm{e}^{\mathrm{aa}}$ and $\Delta\mathbf{D}_\mathrm{e}^{\mathrm{u}}$ are sparse, they would ideally constitute a cheaper calculation in equations 3.40 and 3.41. The updating algorithm for the B-approximation as is illustrated in Figure 4.13.

The A- and B-approximations are very similar; they only differ in the fact that the B-approximation includes the exact contribution from the active-active block of $\mathbf{D}_\mathrm{e}$, thus attempting to capture more of the changes in two-electron interactions. The implementation and testing of the approximations are detailed in Section 4.3.

3.3 Investigation of the different inactive density matrix blocks

The approximations to the differentiated two-electron integral matrix discussed in section 3.2 attempt to exploit the structure of the inactive density to propose an approximate matrix that will be computationally cheaper without much loss of accuracy. For instance, in the A-approximation it was suggested that the change in density between iterations, $\Delta\mathbf{D}_\mathrm{e}$, will only have nonzero elements in a localized region, making it possibly to tailor the construction of $\mathbf{G}^x(\Delta\mathbf{D}_\mathrm{e})$ so that it is computationally cheaper than for a density without such a predictable structure. The approximation is then set up so that only this cheaper calculation is performed in each iteration, with the exception of the first iteration in which the more expensive exact matrix is calculated. Getting a better understanding of the structure of $\mathbf{D}_\mathrm{e}$ and how it changes during the optimization might help to explain the performance of the A- and B-approximations, and may even give some insight into how to devise other approximations. Some calculations have been carried out in this thesis in an attempt to get numerical insight into the behavior of the $\mathbf{G}^x(\mathbf{D}_\mathrm{e})$ matrix. Specifically, these calculations aimed to see whether there are any consistent differences between the different blocks of $\mathbf{D}_\mathrm{e}$ entering the matrix. The calculations were ordinary MLHF geometry optimizations, but the calculation of $\mathbf{G}^x(\mathbf{D}_\mathrm{e})$ was performed with the inactive density split up as

$$\mathbf{G}^x(\mathbf{D}_\mathrm{e}) = \mathbf{G}^x(\mathbf{D}_\mathrm{e}^{\mathrm{aa}}) + \mathbf{G}^x(\mathbf{D}_\mathrm{e}^{\mathrm{ee}}) + \mathbf{G}^x(\mathbf{D}_\mathrm{e}^{\mathrm{mix}}), \tag{3.42}$$

where

$$\mathbf{D}_\mathrm{e}^{\mathrm{aa}} = \begin{pmatrix} \mathbf{aa} & \mathbf{0} \\ \mathbf{0} & \mathbf{0} \end{pmatrix} \tag{3.43}$$

$$\mathbf{D}_\mathrm{e}^{\mathrm{ee}} = \begin{pmatrix} \mathbf{0} & \mathbf{0} \\ \mathbf{0} & \mathbf{ee} \end{pmatrix} \tag{3.44}$$

$$\mathbf{D}_{\mathrm{e}}^{\mathrm{mix}} = \begin{pmatrix} \mathbf{0} & \mathbf{ae} \\ \mathbf{ea} & \mathbf{0} \end{pmatrix}. \tag{3.45}$$

Some properties of these differentiated matrices were printed to see e.g. if some of them consistently contribute more to the gradient, or if some of them consistently change less from one iteration to the next. The specifics of these tests are presented in Section 4.4.

4 Implementation and computational details

4.1 Implementation of the MLHF molecular gradient into the eT program

eT is a newly released open source electronic structure program with a focus on Coupled Cluster and multilevel methods[30]. It features an MO driven MLHF wave function optimization module as described in section 2.3. The MLHF active region is specified by the user by listing the active atoms on input, and the density is decomposed into active and inactive density accordingly. using Cholesky decomposition.

Currently, the only available geometry optimization algorithm in eT uses the RF method with BFGS Hessian updating, all carried out in Cartesian coordinates. The geometry optimization is not compatible with the MLHF wave function in the official release, and so in this thesis a local version of the code was modified to allow MLHF geometry optimization calculations. This included the development of procedures for constructing the MLHF molecular gradient which will be detailed later on in this section. Figure 4.1 illustrates the MLHF geometry optimization algorithm as implemented in eT.

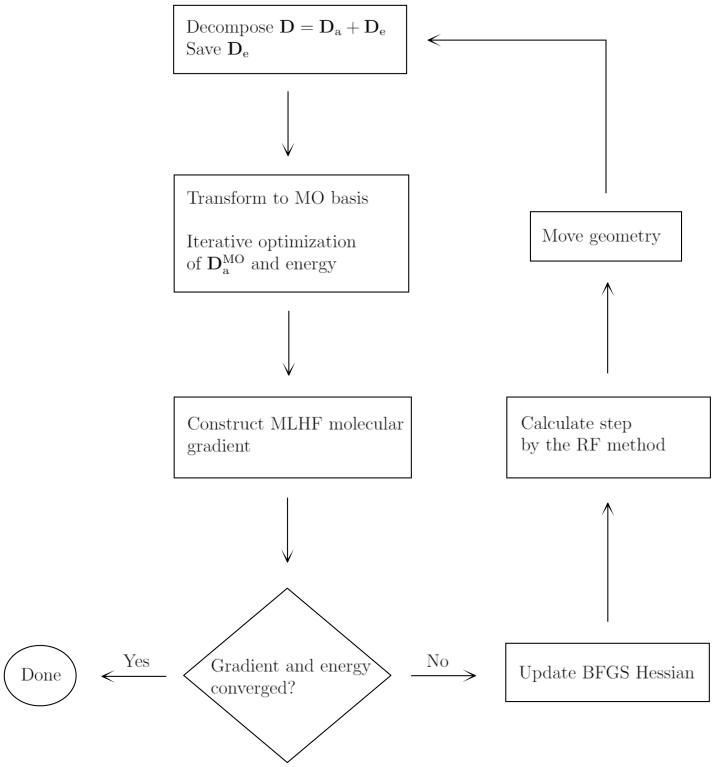

Figure 4.1: Flowchart illustrating the MLHF geometry optimization algorithm as implemented in eT. The algorithm for full space HF geometry optimization is similar, only differing in that it does not include any decomposition of the full density, it performs the HF energy minimization in the AO basis, and it uses the HF molecular gradient.

The implementation of the MLHF molecular gradient needed to be done in such a way as to achieve the property that only a specified, local region of the molecular system is optimized. The nuclei outside this region should never move throughout the procedure, and may be referred to as the *frozen nuclei* or *frozen atoms*. This was achieved by calculating only the gradient elements corresponding to unfrozen nuclei, while setting the elements corresponding to frozen nuclei to zero. In other words, the frozen nuclei were explicitly enforced to not move via the construction of the gradient. The algorithm for the construction of the gradient is illustrated in Figure 4.2.

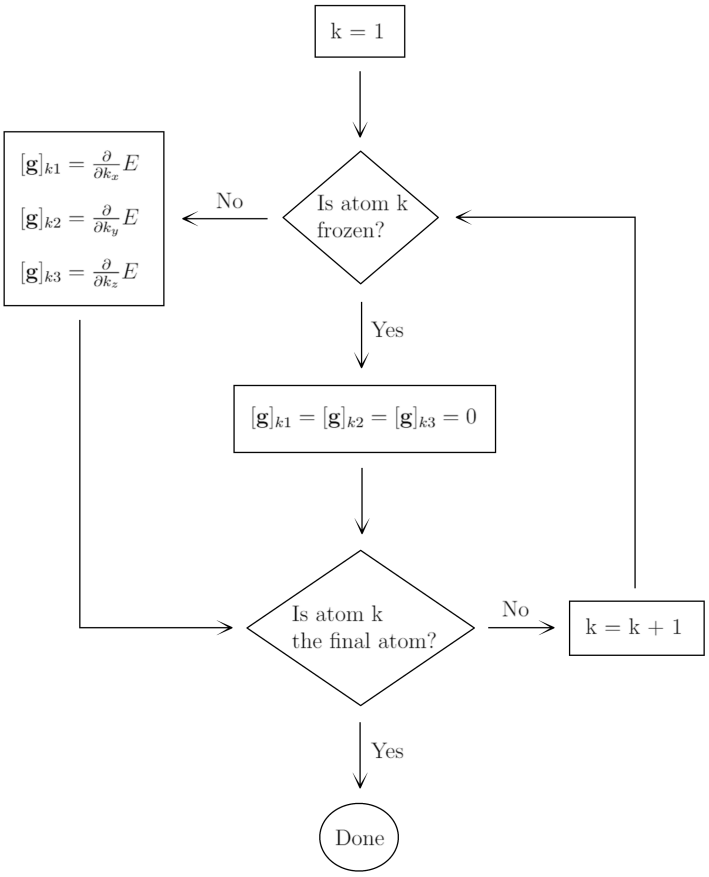

Figure 4.2: Flowchart showing the construction of the molecular gradient with frozen atoms. The label k signifies the current atoms placement in the list, while the second label signifies the spatial coordinate (x, y, z) of that atom.

The method of freezing nuclei is such that the frozen atoms are specified separate from the MLHF active atoms on input. It is thus possible to have atoms which are frozen in space but nonetheless active in the energy minimization. In other words, the MLHF active region may be extended beyond the unfrozen region, or vice-versa. The proof-of-concept calculations presented later will include calculations in which the MLHF active region is extended beyond the geometrically unfrozen region. The frozen atoms method was also implemented for the HF molecular gradient, thus allowing geometry optimization with a HF wave function together with frozen atoms

which, will also feature in the proof-of-concept calculations.

4.2 Proof-of-concept calculations

The proof-of-concept calculations may be categorized into three different classes:

Class 1. Full space HF geometry optimization with no frozen atoms. In other words, a regular HF geometry optimization to be used as a benchmark for the other calculations. The full density is optimized in each iteration, and all atoms are allowed to move.

Class 2. HF geometry optimization with a region of unfrozen atoms surrounded by frozen atoms, hereafter referred to as frozen HF. These calculations use the regular HF geometry optimization algorithm in the eT official release, but with the frozen atoms algorithm (Figure 4.2) implemented for the HF molecular gradient. In other words, the full density is optimized in each iteration, but only unfrozen atoms are allowed to move.

Class 3. MLHF geometry optimization, the algorithm of which is illustrated in Figure 4.1. In each iteration, the active density is optimized while the inactive density is modeled by the SAD starting guess. Only unfrozen atoms are allowed to move. The active atoms are specified on input, and the decomposition into active and inactive space is done accordingly. The frozen atoms are also specified on input, and is achieved through the implementation of the frozen atoms algorithm (Figure 4.2) for the MLHF molecular gradient. Calculations in which the active and unfrozen region are the same, and calculations in which the active region extends beyond the unfrozen region have both been carried out.

The energy of the optimized geometries were determined with a final HF energy minimization.

All calculations have been carried out in the eT program except for the full space HF calculations of Class 1. These were carried out in LSDALTON[29], as convergence proved difficult to achieve in eT. The cc-pVDZ basis set was used for all calculations. The energy and gradient thresholds of the geometry optimization were both set to 10^{-4} a.u. for all calculations. Starting geometries were generated in Avogadro[56] using the MMFF94 force field. The five molecular test systems, of which the first four were used for the proof-of-concept calculations, are:

Molecule 1. Psoralen

Molecule 2. 2-phenyl-4,5-dicyano imidazole, hereafter referred to as PDCI

Molecule 3. Proflavine

Molecule 4. bis(2,4,6-trichlorophenyl) oxalate, hereafter referred to as TCPO

Molecule 5. 1-methyl-2-[2'-(5'-tricyanovinyl)thienyl]-4,5-para-methoxyphenyl imidazole, hereafter referred to as the y-chromophore.

The fifth molecule, the y-chromophore, has been used to test the approximate gradient terms presented in Section 3.2. These tests will later be detailed in Sections 4.3 and 4.4.

Figures 4.3 - 4.7 show the test molecules with the various divisions into regions of different levels of calculation. The blue shaded area indicates the unfrozen atoms which will move during the optimization; the remaining atoms will be stationary. The red circle indicate the MLHF active region; the density associated with the atoms within this circle will be optimized at the HF level, while the density of the outside atoms are modeled with SAD. In terms of the above three classes of calculation, the subfigure (a) of each figure 4.3 - 4.5 shows the Class 2 calculation, while all the other subfigures show calculations that belong to Class 3.

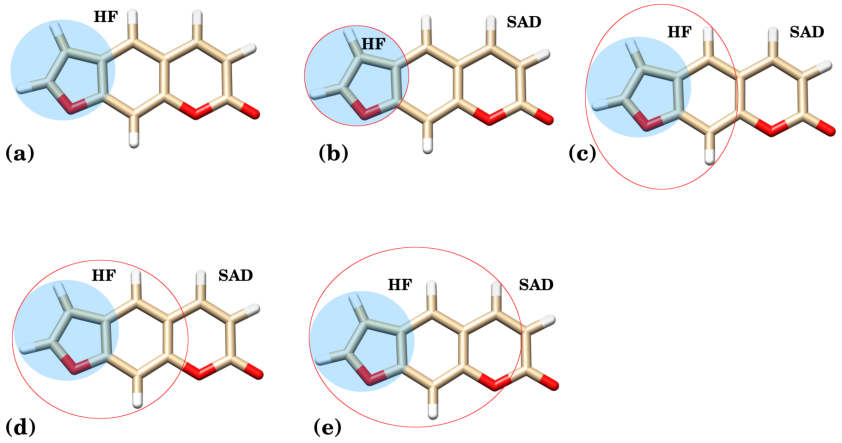

Figure 4.3: The psoralen molecule divided into regions of different levels of calculation. The blue shaded region is the geometrically unfrozen region, while the red region is the MLHF active region. MLHF inactive atoms are modeled with SAD. Subfigure (a) illustrates the frozen HF calculation, where the entire system is optimized at the HF level, but only the blue shaded region is moved during the geometry iterations.

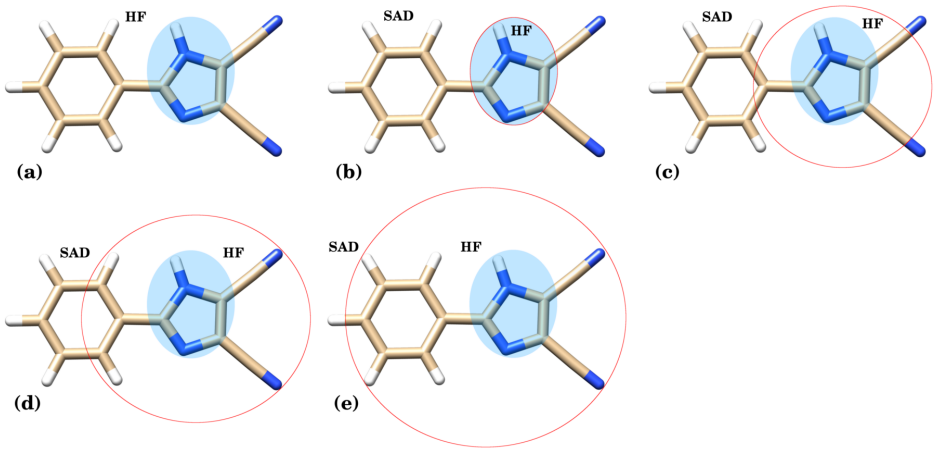

Figure 4.4: The PDCI molecule divided into regions of different levels of calculation. The blue shaded region is the geometrically unfrozen region, while the red region is the MLHF active region. MLHF inactive atoms are modeled with SAD. Subfigure (a) illustrates the frozen HF calculation, where the entire system is optimized at the HF level, but only the blue shaded region is moved during the geometry iterations.

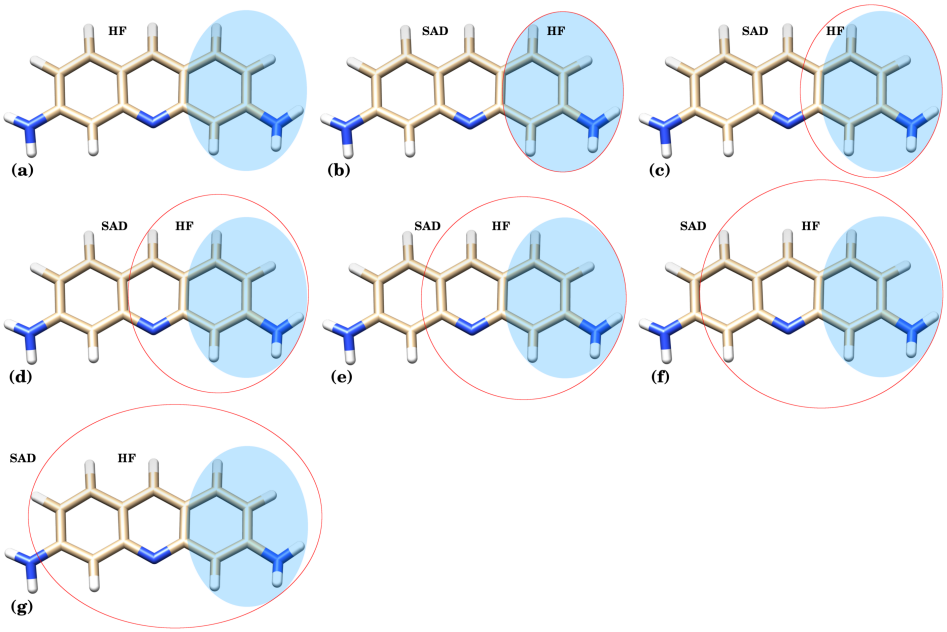

Figure 4.5: The proflavine molecule divided into regions of different levels of calculation. The blue shaded region is the geometrically unfrozen region, while the red region is the MLHF active region. MLHF inactive atoms are modeled with SAD. Subfigure (a) illustrates the frozen HF calculation, where the entire system is optimized at the HF level, but only the blue shaded region is moved during the geometry iterations.

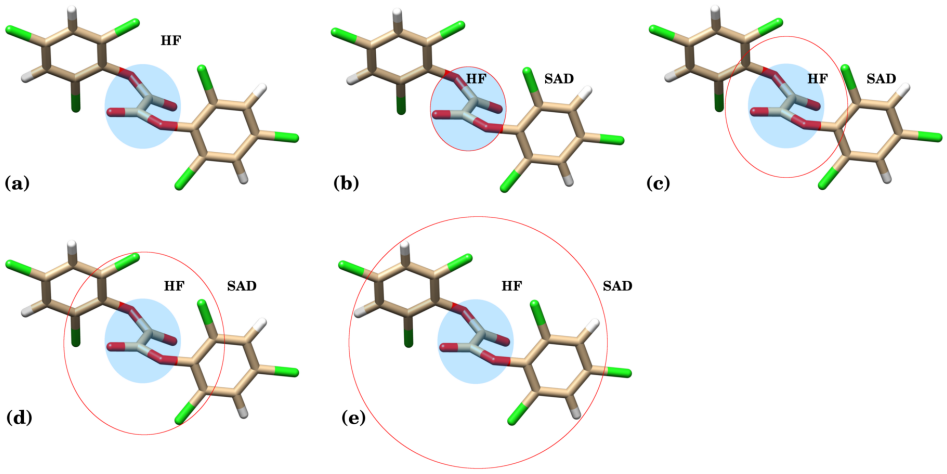

Figure 4.6: The TCPO molecule divided into regions of different levels of calculation. The blue shaded region is the geometrically unfrozen region, while the red region is the MLHF active region. MLHF inactive atoms are modeled with SAD. Subfigure (a) illustrates the frozen HF calculation, where the entire system is optimized at the HF level, but only the blue shaded region is moved during the geometry iterations.

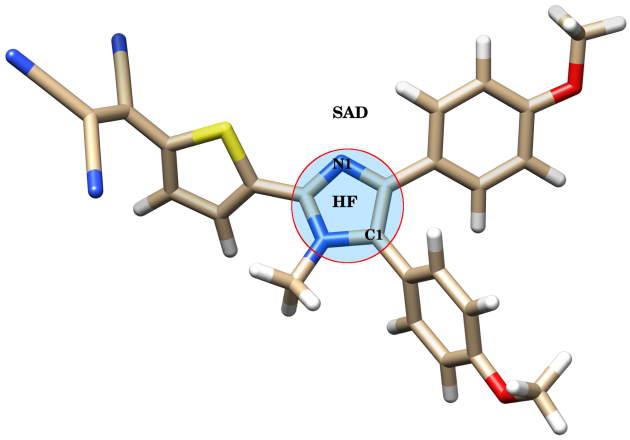

Figure 4.7: The y-chromophore divided into an MLHF active, geometrically unfrozen region indicated by the blue shaded area inside the red circle. The outside atoms are modeled with SAD, and are frozen during the geometry optimization. Two of the active atoms, C1 and N1, are indicated.

A selection of bond lengths and bond angles obtained with the different optimizations will be compared for molecules 1 - 4 to see if there are significant differences between the different geometries. These particular bond lengths and angles are shown in Figures 4.8 - 4.11.

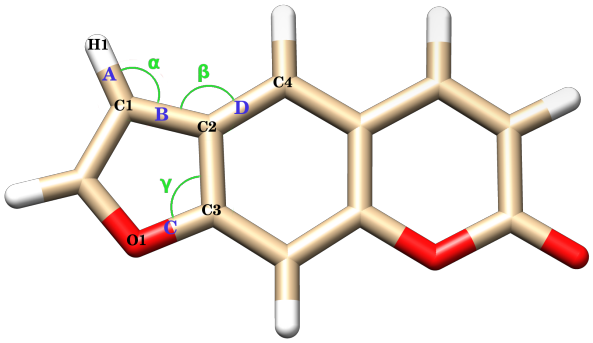

Figure 4.8: A selection of bond lengths (in blue) and bond angles (in green) of the psoralen molecule. They are given by:
A: H1-C1 B: C1-C2 C: O1-C3 D: C2-C4
α: H1-C1-C2 β: C1-C2-C4 γ: O1-C3-C2.

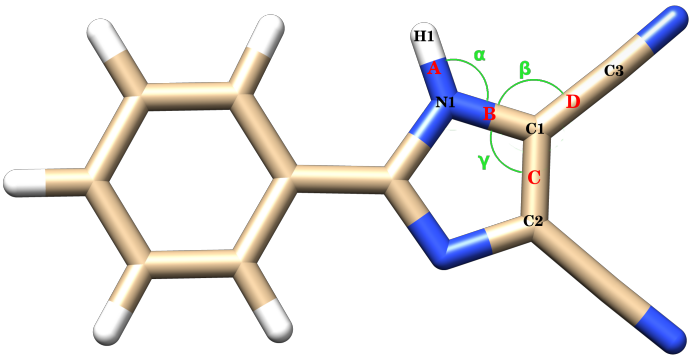

Figure 4.9: A selection of bond lengths (in red) and bond angles (in green) of the PDCI molecule. They are given by:
A: H1-N1 B: C1-N1 C: C1-C2 D: C1-C3
α: H1-N1-C1 β: N1-C1-C3 γ: N1-C1-C2.

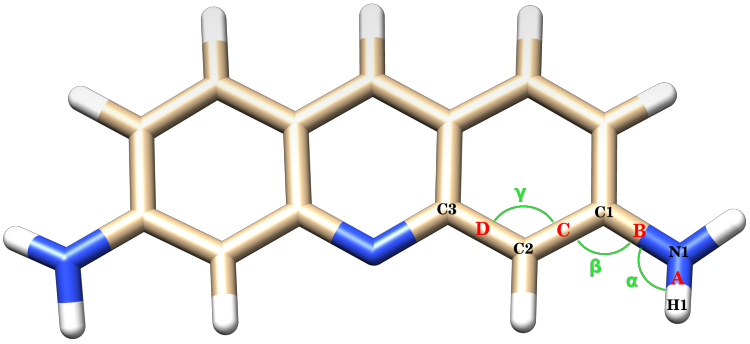

Figure 4.10: A selection of bond lengths (in red) and bond angles (in green) of the proflavine molecule. They are given by:
A: H1-N1 B: C1-N1 C: C1-C2 D: C2-C3
α: H1-N1-C1 β: N1-C1-C2 γ: C1-C2-C3.

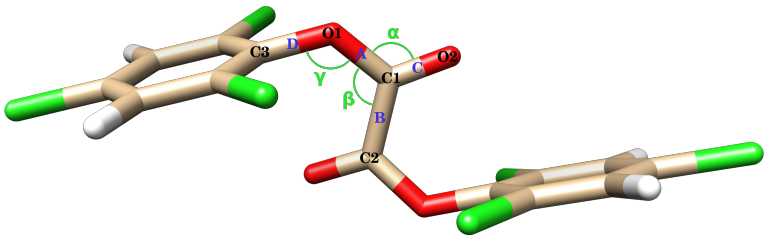

Figure 4.11: A selection of bond lengths (in blue) and bond angles (in green) of the TCPO molecule. They are given by:
A: O1-C1 B: C1-C2 C: C1-O2 D: O2-C3
α: O1-C1-O2 β: O1-C1-C2 γ: C1-O1-C3.

4.3 Implementation and testing of the approximate gradient terms

In Section 3.2 we presented two approximations to the differentiated two-electron integral matrix $\mathbf{G}^x(\mathbf{D}_\mathrm{e})$, dubbed the A- and B-approximations. They are both based on calculating the exact matrix in the first iteration and performing an approximate updating in the subsequent iterations. Figures 4.12 - 4.13 illustrate the updating algorithm of the A- and B-approximations, respectively, as implemented in the MLHF geometry optimization code in eT.

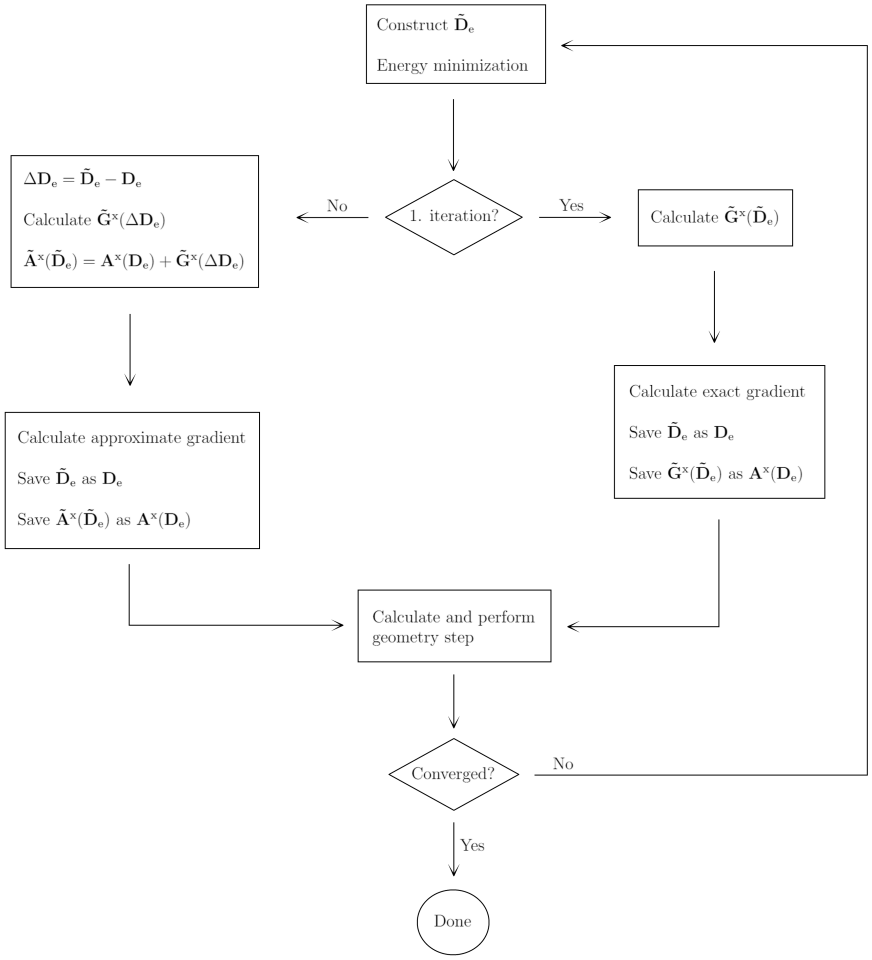

Figure 4.12: Flowchart illustrating the geometry optimization with the approximate differentiated two-electron integral matrix $\mathbf{A}^x(\mathbf{D}_\mathrm{e})$.

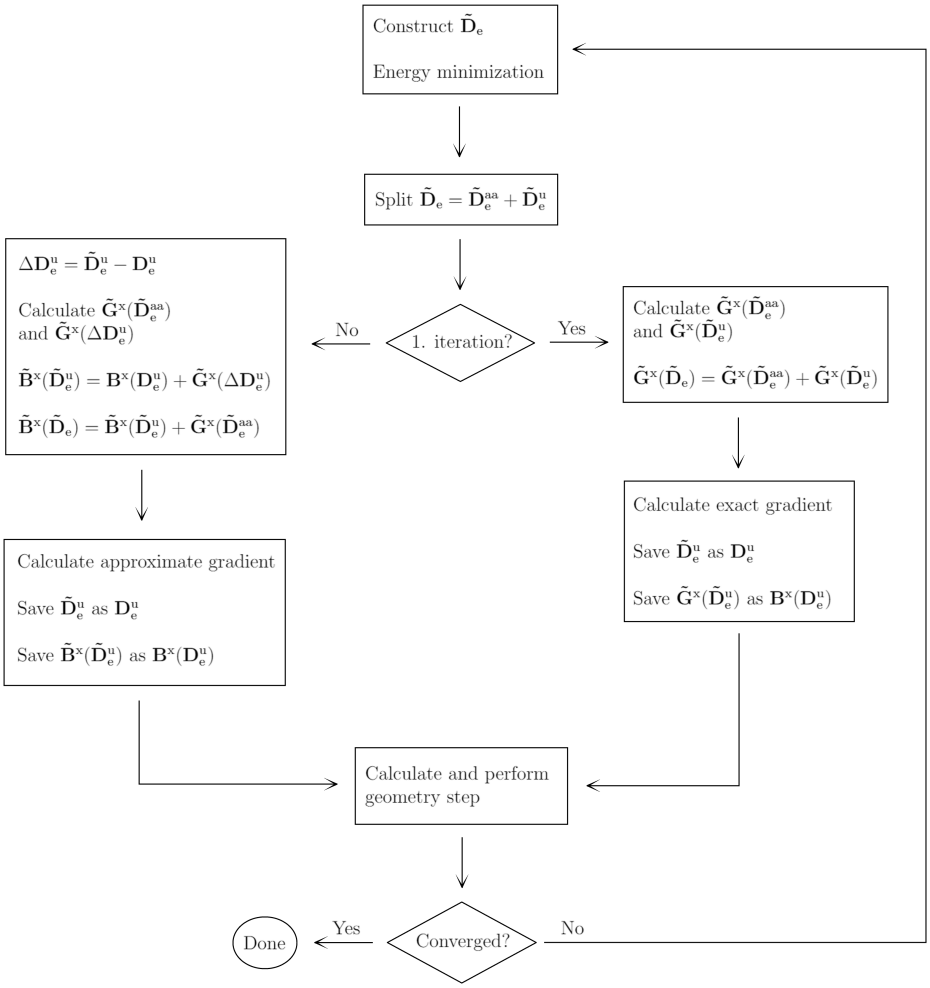

Figure 4.13: Flowchart illustrating the geometry optimization with the approximate differentiated two-electron integral matrix $\mathbf{B}^x(\mathbf{D}_\mathrm{e})$.

The approximations were tested for accuracy by performing MLHF geometry optimization on the y-chromophore test molecule (figure 4.7) and comparing with the exact matrix. Specifically, the following quantities were printed:

- Absmax$[\mathbf{A}^x(\mathbf{D}_\mathrm{e}) - \mathbf{G}^x(\mathbf{D}_\mathrm{e})]$, the absolute maximum of the difference in the matrix.

- Tr$[\mathbf{D}\mathbf{G}^x(\mathbf{D}_\mathrm{e})]$, the trace contribution of the exact matrix.

- Abs$[\mathrm{Tr}[\mathbf{D}\mathbf{A}^x(\mathbf{D}_\mathrm{e})] - \mathrm{Tr}[\mathbf{D}\mathbf{G}^x(\mathbf{D}_\mathrm{e})]]$, the absolute value of the difference in the trace contributions.

The same quantities were printed from the B-matrix. At each iteration we have one of each of these quantities associated with each spatial coordinate of each active atom, in other words $3 \times N_{active}$ of each quantity in total. We therefore restrict the investigation to two of the active atoms of the y-chromophore, a carbon and a nitrogen indicated in Figure 4.7.

4.4 Investigation of the different inactive density matrix blocks

To investigate the different block contributions to the $\mathbf{G}^x(\mathbf{D}_\mathrm{e})$ matrix (equation 3.39), a few quantities related to this matrix were printed for a MLHF geometry optimization of the y-chromophore (figure 4.7). Specifically, for the block term $\mathbf{G}^x(\mathbf{M})$, where $\mathbf{M} \in \{\mathbf{D}_\mathrm{e}^\mathrm{aa}, \mathbf{D}_\mathrm{e}^\mathrm{ee}, \mathbf{D}_\mathrm{e}^\mathrm{mix}\}$, the following quantities were printed:

- Absmax$[\mathbf{G}^x(\mathbf{M})]$, the absolute maximum of the matrix.

- Tr$[\mathbf{D}\mathbf{G}^x(\mathbf{M})]$, the trace contribution from the matrix to the gradient. This will reveal if any of the block terms dominate in the gradient contribution.

- ΔTr$[\mathbf{D}\mathbf{G}^x(\mathbf{M})]$, the change in the trace contribution between two iterations. This will reveal if any of the trace contributions are relatively constant.

As for the investigation of the approximate matrices, we restrict the investigation to two of the active atoms of the y-chromophore. Furthermore, we consider Absmax$[\mathbf{G}^x(\mathbf{M})]$ and Tr$[\mathbf{D}\mathbf{G}^x(\mathbf{M})]$ in only the second iteration, and ΔTr$[\mathbf{D}\mathbf{G}^x(\mathbf{M})]$ as the change between the first and second iterations.

5 Results and discussion

5.1 Proof-of-concept calculations

Tables 5.1 - 5.4 show the HF energies of the optimized geometries of the test systems, the number of active AOs used in the geometry optimization calculations, and the differences in the energies compared to the full space HF (Class 1, see section 4.2) optimized geometry. The row labels denote the partitioning of the system as dictated by the corresponding subfigure in figures 4.3 - 4.6. For example, (a) is always the frozen HF geometry (Class 2), while (b) and onwards are the MLHF geometries (Class 3) with varying active spaces indicated by the listed active AO number.

Geometry	HF energy [a.u.]	Deviation [a.u.]	Active/Total AOs
Full space HF	-644.67838	-	-
Frozen HF (a)	-644.66863	0.00975	-
MLHF (b)	-644.66725	0.01113	96/226
MLHF (c)	-644.66717	0.01121	138/226
MLHF (d)	-644.66709	0.01129	166/226
MLHF (e)	-644.66714	0.01124	198/226

Table 5.1: The HF energy of psoralen at equilibrium geometries obtained with full space HF, frozen HF, and different sized MLHF. The number of active AOs in the MLHF calculations and the deviation in energy compared to the full space HF optimized geometry is also included.

Geometry	HF energy [a.u.]	Deviation [a.u.]	Active/Total AOs
Full space HF	-637.88549	-	-
Frozen HF (a)	-637.88140	0.00409	-
MLHF (b)	-637.88009	0.00540	93/240
MLHF (c)	-637.87957	0.00592	143/240
MLHF (d)	-637.87962	0.00587	203/240
MLHF (e)	-637.87968	0.00581	240/240

Table 5.2: The HF energy of PDCI at equilibrium geometries obtained with full space HF, frozen HF, and different sized MLHF. The number of active AOs in the MLHF calculations and the deviation in energy compared to the full space HF optimized geometry is also included.

Geometry	HF energy [a.u.]	Deviation [a.u.]	Active/Total AOs
Full space HF	-662.11563	-	-
Frozen HF (a)	-662.10632	0.00931	-
MLHF (b)	-662.10406	0.01157	112/279
MLHF (c)	-662.10459	0.01104	143/279
MLHF (d)	-662.10447	0.01116	176/279
MLHF (e)	-662.10431	0.01132	206/279
MLHF (f)	-662.10394	0.01169	243/279
MLHF (g)	-662.10385	0.01178	269/279

Table 5.3: The HF energy of proflavine at equilibrium geometries obtained with full space HF, frozen Hf, and different sized MLHF. The number of active AOs in the MLHF calculations and the deviation in energy compared to the full space HF optimized geometry is also included.

Geometry	HF energy [a.u.]	Deviation [a.u.]	Active/Total AOs
Full space HF	-3588.97588	-	-
Frozen HF (a)	-3588.97084	0.00504	-
MLHF (b)	-3588.96769	0.00819	102/380
MLHF (c)	-3588.96705	0.00883	139/380
MLHF (d)	-3588.96510	0.01078	284/380
MLHF (e)	-3588.96503	0.01085	366/380

Table 5.4: The HF energy of TCPO at equilibrium geometries obtained with full space HF, frozen HF, and different sized MLHF. The number of active AOs in the MLHF calculations and the deviation in energy compared to the full space HF optimized geometry is also included.

Figures 5.1 - 5.4 show the HF energies of the optimized geometries of the tests systems plotted against the number of active AOs used in the geometry optimization, as listed in the corresponding Tables 5.1 - 5.4. For full space HF and frozen HF, the number of active AOs is defined as the number of total AOs.

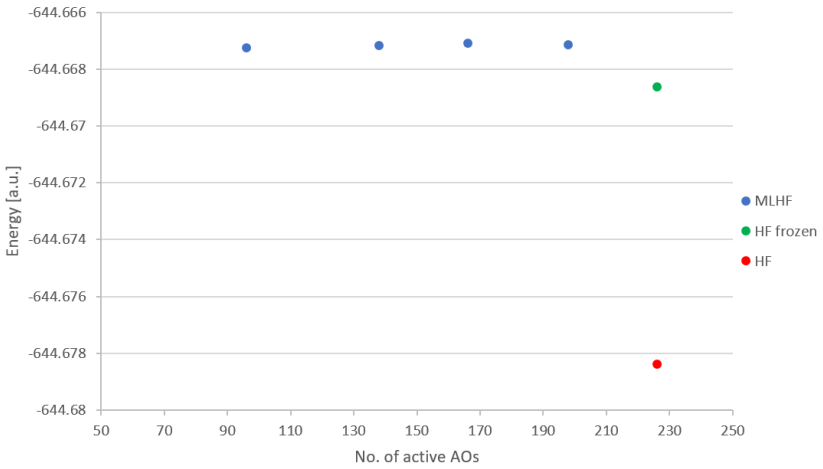

Figure 5.1: The HF energy of psoralen at geometries optimized with different sized MLHF, frozen nuclei HF, and full space HF, plotted against the number of active AOs.

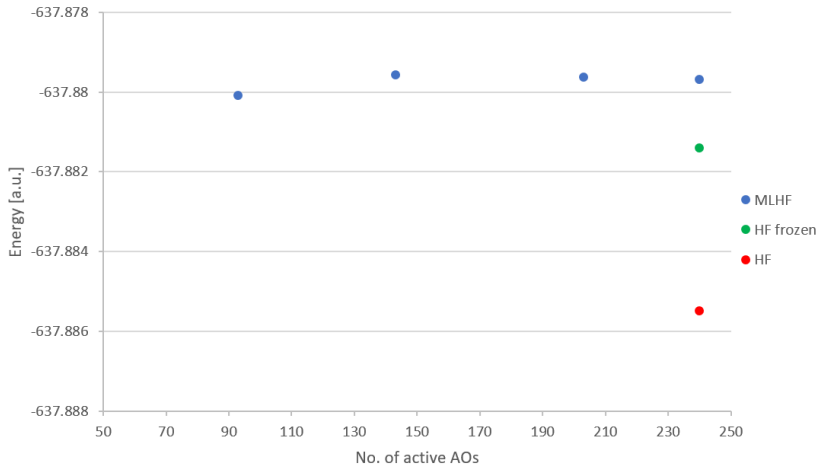

Figure 5.2: The HF energy of PDCI at geometries optimized with different sized MLHF, frozen nuclei HF, and full space HF, plotted against the number of active AOs.

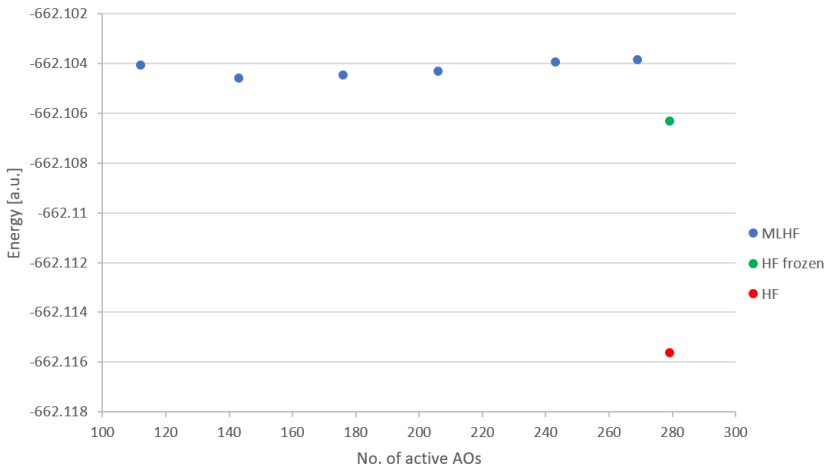

Figure 5.3: The HF energy of proflavine at geometries optimized with different sized MLHF, frozen nuclei HF, and full space HF, plotted against the number of active AOs.

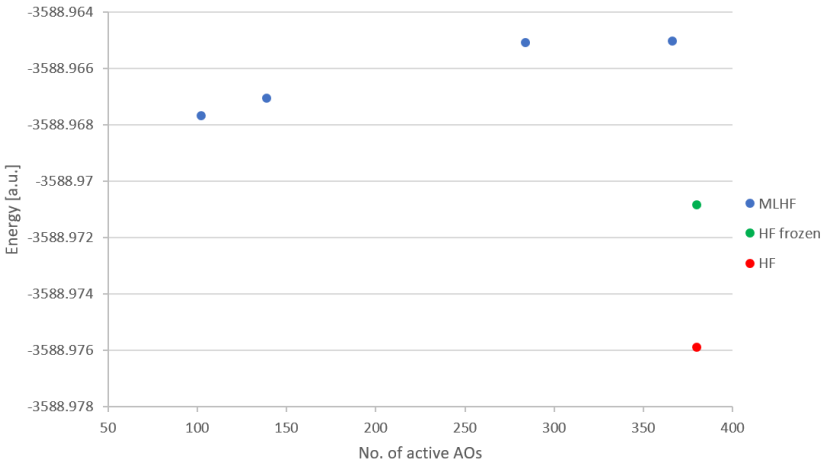

Figure 5.4: The HF energy of TCPO at geometries optimized with different sized MLHF, frozen nuclei HF, and full space HF, plotted against the number of active AOs.

Tables 5.5 - 5.8 show bond lengths and bond angles of geometries obtained with frozen HF and MLHF calculations for molecules 1 - 4. These bond lengths and angles are illustrated in the corresponding Figures 4.8 - 4.11.

Geometry	A [Å]	B [Å]	C [Å]	D [Å]	α [°]	β [°]	γ [°]
Frozen HF (a)	1.077	1.455	1.343	1.385	128.14	135.86	110.38
MLHF (b)	1.098	1.465	1.354	1.395	127.74	136.39	109.77
MLHF (e)	1.098	1.467	1.358	1.394	127.74	136.24	109.64

Table 5.5: Comparison between a selection of bond lengths and angles obtained with frozen HF and two different sized MLHF calculations, for the psoralen molecule.

Geometry	A [Å]	B [Å]	C [Å]	D [Å]	α [°]	β [°]	γ [°]
Frozen HF (a)	0.997	1.373	1.363	1.432	125.13	104.65	123.95
MLHF (b)	0.993	1.359	1.375	1.435	124.94	105.72	125.15
MLHF (e)	0.982	1.351	1.367	1.428	124.77	105.75	125.02

Table 5.6: Comparison between a selection of bond lengths and angles obtained with frozen HF and two different sized MLHF calculations, for the PDCI molecule.

Geometry	A [Å]	B [Å]	C [Å]	D [Å]	α [°]	β [°]	γ [°]
Frozen HF (a)	1.001	1.390	1.359	1.432	113.90	122.97	120.86
MLHF (b)	1.006	1.367	1.377	1.445	115.52	122.52	121.44
MLHF (g)	1.010	1.366	1.379	1.444	115.65	122.51	120.74

Table 5.7: Comparison between a selection of bond lengths and angles obtained with frozen HF and two different sized MLHF calculations, for the proflavine molecule.

Geometry	A [Å]	B [Å]	C [Å]	D [Å]	α [°]	β [°]	γ [°]
Frozen HF (a)	1.339	1.543	1.172	1.371	119.87	118.16	128.16
MLHF (b)	1.311	1.557	1.166	1.372	120.59	121.35	127.36
MLHF (e)	1.296	1.551	1.163	1.363	121.24	121.16	128.92

Table 5.8: Comparison between a selection of bond lengths and angles obtained with frozen HF and two different sized MLHF calculations, for the TCPO molecule.

5.1.1 Energy comparison

The full space HF (Class 1, see section 4.2) geometry is of significantly lower energy than the frozen HF (Class 2) and MLHF (Class 3) geometries. This is to be expected considering the latter two are only optimized in a smaller region of the geometry. This energy difference is on the order of 10^{-2} Hartree except for the PDCI molecule, where it is on the order of 10^{-3} Hartree.

Comparing the frozen HF and MLHF geometries is especially interesting because

they optimize the same geometrical region, but use different wave functions. The energy of the frozen HF geometry is always lower than for the MLHF geometries, but this difference is on the order of 10^{-3} Hartree. The TCPO molecule is an exception; for this molecule, the MLHF geometries are noticeably different in energy compared to the other molecules, and this will be addressed later. Since the energy threshold was set to 10^{-4} Hartree in the geometry optimization, the difference in the energy of frozen HF geometries and MLHF geometries is not the result of numerical variations. This means that even though the unfrozen region is the same, the presence of an unoptimized density in the frozen region affects the convergence and leads to a geometry of higher energy. This makes sense since the HF and MLHF wave functions, being different, result in different PES's with differently located minima. The minimum of the MLHF PES will necessarily (unless the two minima are far apart) have to correspond to a point on the HF PES that is higher in energy than the HF PES minimum. In other words, the HF energy will be higher for a MLHF geometry. It does however appear that this energy difference will be small compared to the deviation from the energy of the full space HF geometry.

5.1.2 Effects of extending the active space

From the above discussion that a difference in the wave function result in a shift of the PES minimum, it would seem intuitive that the MLHF geometries would approach the frozen HF geometry as the active space is extended. We would expect that as the active space increases and the MLHF wave function converges to the HF wave function, the MLHF PES would also converge to the HF PES. After all, the frozen HF calculation should correspond to a MLHF calculation in which all atoms are active. Surprisingly, this is not the case for our calculations; the energy of MLHF geometries do not approach the energy of the frozen HF geometry, and in most cases it actually increases slightly for larger active spaces. One particularly noteworthy case is the MLHF (e) calculation of the PDCI system, where the density has been decomposed in such a way that the number of active AOs equals the number of total AOs (Table 5.2). It still does not coincide with the frozen HF geometry. The reason for this lack of convergence to the frozen HF geometry with increasing active space is unclear. It could be a result of the MLHF wave function not converging to the HF wave function as it should in theory, and this would indicate an oversight in the implementation of the method. It could also be the case that the assumption that the MLHF PES will converge to the HF PES is incorrect, but this assumption seems to follow from the aforementioned convergence of the wave function. Finally, it could be that the MLHF geometry optimizations are locating a different local minimum entirely. It is highly unlikely that any of the calculations have converged to saddle points because the BFGS Hessian updating should ensure a positive definite Hessian and convergence to a minimum.

The different MLHF geometries are quite similar in energy, differing at most on the order of only 10^{-4} Hartree, with the TCPO molecule as an exception. This suggests that the extension of the active space does not have a large effect on the convergence of the unfrozen region. In other words, that the optimization is not very sensitive to whether or not the density of the immediate surroundings is optimized. For the TCPO molecule, the largest deviations in energy between the different MLHF geometries is on the order of 10^{-3} Hartree, indicating that the optimization of this molecule is more sensitive to the inactive density. Maybe the low rigidity of the

freely rotatable single bonds at the border between the frozen and unfrozen regions of the TCPO system (see Figure 4.6) means that the unfrozen region is more easily affected by the density of the trichlorophenyl groups, but this is just speculation. In any case, it appears that the extension of the active space either doesn't change the energy significantly, or it increases the energy. For this reason we will from now on focus mostly on MLHF (b), the MLHF calculation with the smallest active space.

5.1.3 Comparing bond lengths and bond angles

As previously discussed, the frozen HF geometry and MLHF geometry will be different due to a shift of the PES minimum, as evidenced by their difference in energy. This is further seen from the differences in the selection of bond lengths and angles of these geometries. Almost all of the differences in bond lengths between frozen HF and MLHF (b) are within 2 pm, while almost all of the differences in bond angles are within 1°. Again, the TCPO molecule is a notable exception, with a difference in bond length A of 2.8 pm and a difference in angle β of 2.55°. A closer look at the two TCPO geometries showed a noticeable twisting of the oxalate unit (see Figure 4.6) for the MLHF geometry, which further adds to the aforementioned speculation that low rigidity might be a factor for the sensitivity to an unoptimized environment.

Further comparing the frozen HF and MLHF (b) geometries, the average bond difference across all molecules is 1.2 pm, while the average angle difference is 0.91°. In general, HF geometries usually differ from the exact equilibrium geometries by a couple of pm in bond lengths and a couple of degrees in bond angles, so these results are within the usual performance of HF.

For the MLHF geometry with the largest active space (MLHF (g) for proflavine and MLHF (e) for the other molecules), the deviation from frozen HF is larger than for the MLHF (b) geometry for a majority of the bond lengths and angles. Here, the average bond difference is 1.5 pm, while the average angles difference is 0.90°. This shows further that the extension of the active space does not yield geometries that approach the frozen HF geometry.

It should be emphasized that these comparisons are all done within the HF level of theory. To properly assess the quality of the MLHF geometry optimization, comparisons with more accurate (or exact) structures are needed. A more extensive study, featuring several different methods, a variety of test systems, and more types of internal coordinates such as torsion angles, would give a clearer picture of the performance of the method. Still, it is meaningful that the MLHF method seems to lie within the usual quality of HF theory for geometry optimization, as its ultimate goal is to be used as a starting point for more accurate methods.

5.1.4 Orbital reduction and accuracy compromise

We have seen that the MLHF (b) calculation results in a slightly different geometry to the frozen HF (a) geometry, with slightly higher energy. In the psoralen system, we get a reduction in active AOs of 130 for an energy increase of $1.38 \cdot 10^{-3}$ Hartree when going from (a) to (b). For PDCI, a reduction of 147 AOs for an increase of $1.31 \cdot 10^{-3}$ Hartree. For proflavine, a reduction of 167 AOs for an increase of $2.26 \cdot 10^{-3}$ Hartree. Finally for TCPO, a reduction of 278 AOs for an increase of

$3.15 \cdot 10^{-3}$ Hartree. The changes in bond lengths and angles are within the usual error thresholds of HF theory. In total, the MLHF geometry optimization method offers a large computational reduction over the frozen HF method with a seemingly modest loss of accuracy. This seems promising for the application of this method as a cheap starting point for post-HF calculations of molecular properties.

5.1.5 Final considerations

This thesis has not explored the use of different basis sets; only the cc-pVDZ basis has been used. The literature reports that larger basis sets do not improve the HF description of equilibrium geometries because HF underestimates bond lengths as a fundamental result of lacking electron correlation. The HF description can only be improved by first including correlation through a post-HF method. Nevertheless, it would be interesting to study the effects of different basis sets on the MLHF geometry optimization method to see if a more accurate basis can reduce the deviation of the MLHF geometries from the frozen HF geometries. If the MLHF description is significantly improved, the use of a larger basis might be worthwhile since the MLHF method, with its substantially reduced cost, can afford more expensive basis sets. It would also be interesting to compare MLHF geometries and frozen HF geometries against experimental or highly accurate computational results. As mentioned in Section 2.9, results for computationally obtained geometries in general depend on both the amount of electron correlation included and the accuracy of the basis set, and the cancellation of errors between these two aspects can in some cases lead to unforeseen performance. It is therefore not impossible that a comparison with experimental results will reveal MLHF to actually obtain more accurate geometries than frozen HF through some fortunate cancellation of errors. Even if this is not the case, it is nonetheless important to evaluate the accuracy of MLHF geometries not just against regular HF, but also against exact geometries.

It is important to note that the tests systems used in this thesis are nowhere near the system sizes for which the MLHF method is intended. Additionally, the difference in size between the frozen and unfrozen regions in these tests is not very pronounced; in a geometry optimization of an enzyme, for example, the unfrozen active site region would only constitute dozens to a few hundred atoms out of a total of several thousand atoms. Lastly, the unfrozen regions were chosen quite arbitrarily; in a study of actual molecular or chemical properties the unfrozen region would be appropriately selected for the property in question. In short, the proof-of-concept calculations are not quite representative of the calculations one would want to use the method for, but nevertheless shows that the large reduction in computational cost for a modest loss of accuracy seems to work in concept.

5.2 Approximations of the differentiated two-electron integral matrices

This section presents the results of the MLHF calculations carried out with the matrices $\mathbf{A}^x(\mathbf{D}_\mathrm{e})$ and $\mathbf{B}^x(\mathbf{D}_\mathrm{e})$ (see section 3.2) as approximations to $\mathbf{G}^x(\mathbf{D}_\mathrm{e})$. Tables 5.9 and 5.10 show various quantities related to these matrices. Table 5.12 shows the

molecular gradient obtained with the A- and B-approximations alongside the exact gradient. For comparison purposes, the values of the different terms in the exact molecular gradient (equation 3.27) are listed in table 5.11. In all of these tables, the quantities were obtained in the second geometry optimization of the y-chromophore, and are listed for each spatial coordinate of two of the active atoms, a carbon and a nitrogen.

	Absmax diff	Exact trace	Abs trace diff	Abs trace error [%]
C1				
x	0.55812	0.75286	0.24731	32.849
y	0.34469	0.84530	0.07807	9.236
z	0.82504	-0.37528	0.10665	28.419
N1				
x	0.87060	-0.23624	0.26665	112.873
y	0.33530	1.11291	0.07923	7.119
z	0.69889	1.13090	0.40986	36.242

Table 5.9: Errors associated with the approximate matrix $\mathbf{A}^x(\mathbf{D}_\mathrm{e})$ for two of the active atoms of the y-chromophore in the second iteration. All quantities except the percentage error are in atomic units.
Absmax diff = absmax$[\mathbf{A}^x(\mathbf{D}_\mathrm{e}) - \mathbf{G}^x(\mathbf{D}_\mathrm{e})]$
Exact trace = Tr$[\mathbf{D}\mathbf{G}^x(\mathbf{D}_\mathrm{e})]$
Abs trace diff = abs$[\mathrm{Tr}[\mathbf{D}\mathbf{A}^x(\mathbf{D}_\mathrm{e})] - \mathrm{Tr}[\mathbf{D}\mathbf{G}^x(\mathbf{D}_\mathrm{e})]]$
Abs trace error = abs [(trace diff)/(exact trace)$\times$100]

	Absmax diff	Exact trace	Abs trace diff	Abs trace error [%]
C1				
x	0.52992	0.75286	0.28108	37.335
y	0.34468	0.84530	0.07965	9.423
z	0.78309	-0.37528	0.13491	35.949
N1				
x	0.83636	-0.23624	0.30796	130.359
y	0.32189	1.11291	0.09753	8.764
z	0.67279	1.13090	0.45680	40.393

Table 5.10: Errors associated with the approximate matrix $\mathbf{B}^x(\mathbf{D}_\mathrm{e})$ for two of the active atoms of the y-chromophore in the second iteration. All quantities except the percentage error are in atomic units.
Absmax diff = absmax$[\mathbf{B}^x(\mathbf{D}_\mathrm{e}) - \mathbf{G}^x(\mathbf{D}_\mathrm{e})]$
Exact trace = Tr$[\mathbf{D}\mathbf{G}^x(\mathbf{D}_\mathrm{e})]$
Abs trace diff = abs$[\mathrm{Tr}[\mathbf{D}\mathbf{B}^x(\mathbf{D}_\mathrm{e})] - \mathrm{Tr}[\mathbf{D}\mathbf{G}^x(\mathbf{D}_\mathrm{e})]]$
Abs trace error = abs [(trace diff)/(exact trace)$\times$100]

	$2\mathrm{Tr}[\mathbf{D}\mathbf{h}^x]$	$-2\mathrm{Tr}[\mathbf{D}\mathbf{S}^x\mathbf{D}\mathbf{F}_{\mathrm{eff}}]$	$\mathrm{Tr}[\mathbf{D}\mathbf{G}^x(\mathbf{D}_{\mathrm{a}})]$	$\mathrm{Tr}[\mathbf{D}\mathbf{G}^x(\mathbf{D}_{\mathrm{e}})]$	h^x_{nuc}
C1					
x	7.42931	-0.16158	-5.26789	0.75286	-2.74852
y	-1.33347	0.04115	-0.01671	0.84530	0.45755
z	15.60445	-0.08552	-10.54626	-0.37528	-4.60312
N1					
x	3.11470	-0.01518	-1.56006	-0.23624	-1.30585
y	-9.81960	0.05811	4.36643	1.11291	4.28378
z	-40.11636	0.41153	23.51456	1.13090	15.06439

Table 5.11: Contributions from the different terms of the exact molecular gradient, for two of the active atoms of the y-chromophore in the second iteration. All quantities are in atomic units.

	A grad	B grad	Exact grad
C1			
x	-0.24311	-0.27689	0.00419
y	0.07187	0.07350	-0.00617
z	-0.11245	-0.14075	-0.00573
N1			
x	-0.26929	-0.31060	-0.00262
y	-0.07748	-0.09584	0.00163
z	-0.40480	-0.45169	0.00502

Table 5.12: Comparison of the gradient obtained with the A- and B-approximations and with the exact method, for two of the active atoms of the y-chromophore in the second iteration. All quantities are in atomic units.

5.2.1 Accuracy of the A- and B-approximations

The trace contributions from both of the approximate matrices deviate significantly from that of the exact matrix, resulting in approximate gradients that differ from the exact gradient by several orders of magnitude (table 5.12). The reason why the distortion of the gradient is this immense can be understood by looking at the individual contributions to the gradient. These are all several orders of magnitude larger than the gradient itself, meaning that the different contributions must cancel each other out almost completely. In fact, this illustrates the nature of the interplay between different forces within a molecular system. Large attraction and repulsion forces are always present between the particles, but balance each other at stable geometries. Close to an equilibrium there is only a small net force, corresponding to the negative of the gradient, pointing in the direction of the stationary. However, the use of one of the approximate matrices introduces a deviation on the same scale as these force contributions, and with nothing to cancel it, the resulting approximate gradient is almost equal to the deviation. Unsurprisingly, the active energy was seen to diverge away from the active energy of the geometry obtained with the exact gradient. Both the A- and B-approximations are clearly unusable.

The approximations were built on the assumption that the change in the inactive density will capture most of the changes in two-electron interactions when moving from one geometry to the next. This assumption allowed for types of approximations that were relatively simple to state and implement, not requiring any alterations of the inner workings of the code that calculates the differentiated two-electron integrals. The fact that large deviations are already present in the 2nd iteration shows that they are not the result of an accumulation of tiny errors over several steps, but that our assumption is invalid to the point of throwing the entire optimization out of balance. Future efforts into the reduction of the cost of the differentiated two-electron integral matrix should examine more closely its structure and the interactions involved in order to identify negligible contributions such as e.g. small long-range interactions. Some form of efficient screening method might be possible.

5.3 Investigations of the different inactive density matrix blocks

This section presents quantities related to the different block terms of the differentiated two-electron integral matrix as detailed in Section 4.4. Tables 5.13 and 5.14 list the absmax and the trace contributions of these matrices, respectively, for the second iteration of the MLHF geometry optimization. Table 5.15 lists the change in the trace contributions between the first and second iteration. All quantities are listed for each spatial coordinate of two of the active atoms of the y-chromophore shown in Figure 4.7.

	Absmax $\mathbf{G}^x(\mathbf{D}_\mathrm{e}^\mathrm{aa})$	Absmax $\mathbf{G}^x(\mathbf{D}_\mathrm{e}^\mathrm{ee})$	Absmax $\mathbf{G}^x(\mathbf{D}_\mathrm{e}^\mathrm{mix})$
C1			
x	0.47999	9.24910	0.05972
y	0.35246	6.61866	0.04011
z	0.61305	9.86173	0.07215
N1			
x	0.40124	9.34990	0.03937
y	0.24523	5.08253	0.02060
z	0.35811	8.16368	0.05422

Table 5.13: Comparison of the absmax of the differentiated two-electron integral matrices for different blocks of the inactive density, for two of the active atoms of the y-chromophore in the second iteration. All quantities are in atomic units.

	$\mathrm{Tr}[\mathbf{D}\mathbf{G}^x(\mathbf{D}_\mathrm{e}^\mathrm{aa})]$	$\mathrm{Tr}[\mathbf{D}\mathbf{G}^x(\mathbf{D}_\mathrm{e}^\mathrm{ee})]$	$\mathrm{Tr}[\mathbf{D}\mathbf{G}^x(\mathbf{D}_\mathrm{e}^\mathrm{mix})]$
C1			
x	-1.44716	1.71545	1.23736
y	1.38748	0.78508	-0.48198
z	0.63457	-1.66969	0.28411
N1			
x	1.21467	-1.79676	0.10978
y	-0.41616	2.68286	-0.04093
z	-4.46821	6.93751	-0.20755

Table 5.14: Comparison of the trace contribution of the differentiated two-electron integral matrices for different blocks of the inactive density, for two of the active atoms of the y-chromophore in the second iteration. All quantities are in atomic units.

	$\Delta\mathrm{Tr}[\mathbf{D}\mathbf{G}^x(\mathbf{D}_\mathrm{e}^\mathrm{aa})]$	$\Delta\mathrm{Tr}[\mathbf{D}\mathbf{G}^x(\mathbf{D}_\mathrm{e}^\mathrm{ee})]$	$\Delta\mathrm{Tr}[\mathbf{D}\mathbf{G}^x(\mathbf{D}_\mathrm{e}^\mathrm{mix})]$
C1			
x	-0.18989	0.31173	-0.01862
y	-0.01031	-0.02189	0.05693
z	-0.08193	0.13899	0.02169
N1			
x	0.08885	0.04190	0.09295
y	-0.06751	0.14578	-0.01002
z	-0.16332	0.47563	0.02972

Table 5.15: Comparison of the change from the first to the second iteration in trace contribution of the differentiated two-electron integral matrices for different blocks of the inactive density, for two of the active atoms of the y-chromophore. In other words, $\Delta\mathrm{Tr}[\mathbf{D}\mathbf{G}^x(\mathbf{M})] = \mathrm{Tr}[\mathbf{D}\tilde{\mathbf{G}}^x(\tilde{\mathbf{M}})] - \mathrm{Tr}[\mathbf{D}\mathbf{G}^x(\mathbf{M})]$, where $\mathbf{G}^x(\mathbf{M})$ and $\tilde{\mathbf{G}}^x(\tilde{\mathbf{M}})$ are the matrices in the first and second iteration, respectively. All quantities are in atomic units.

There seems to be no significant difference in the magnitude of the trace contributions from the different inactive density blocks, nor in the magnitude of the change in these contributions between iterations. Interestingly, the absmax of the matrices seems to differ quite consistently, with the aa-matrix an order of magnitude larger than the mix-matrix, and the ee-matrix an order of magnitude larger than the aa-matrix. It is difficult propose explanations for this without any further insight into the matrix structure, and ultimately it does not seem to affect the final gradient contribution. Based on these observations as well as the pathological behaviour of the approximate matrices discussed in Section 5.2, it does not seem worthwhile to further investigate the matrix based on the block structure of the inactive densities or devise approximations accordingly.

6 Summary and conclusions

This thesis has implemented and tested a MLHF wave function for use in the optimization of equilibrium geometries. The two-level MLHF method divides the molecular system into an active and inactive part through a decomposition of the density. Only the active density is optimized at the HF level, while the inactive density remains at the level of the SAD starting guess.

The MLHF molecular gradient was derived in the AO basis, and turned out equivalent to the gradient of the full-space HF model. The gradient was implemented for second order geometry optimization in the eT program using the RF method with BFGS Hessian updating in Cartesian coordinates. A manipulation of the gradient was used to explicitly freeze the environment region in space during geometry optimization, by setting the gradient elements corresponding to the inactive atoms of the environment to zero. A similar freezing technique can be employed for optimizations using the full space HF wave function. In comparing these, the proof-of-concept calculations showed that the MLHF method can achieve a large reduction in the number of optimized AOs for a modest loss in the accuracy of the geometry. The presence of an unoptimized density outside the unfrozen region changes the final geometry to some extent, but the increase in energy and change in bond lengths and angles is within the error thresholds usually seen for HF theory. One of the test systems showed more noticeable geometrical changes, and points to the possibility that low rigidity across the borders might make the dependence on the unoptimized density more pronounced. However, this can not be stated conclusively without more testing. Contrary to what was expected from the theory, the MLHF geometries did not approach the frozen HF geometry for increasing active space sizes. No conclusive reason for this could be determined, and it might point to an oversight in the implementation.

Results have only been obtained within the HF level of theory, and no comparisons to experimental or more accurately modelled geometries have been done. Additionally, the tests systems used were small and in many ways not representative of the large target calculations for this method. However, within these limitations, the results seem promising. They suggest that the MLHF model may prove successful for performing geometry optimization on localized regions of large systems at massively reduced cost, providing a cheap starting point for more accurate models with which the calculation of local properties like core excitations or the modeling of local processes such as enzymatic catalysis can be carried out.

The molecular gradient contains a term of differentiated two-electron integrals which poses a challenge for the efficient implementation of the model. Two simple approximations of this term were formulated without any strong theoretical motivations behind them, but it was found that the delicate balance between the forces of the system, as represented by the gradient, was buckled by these approximations, resulting in gross distortions of the gradient and no convergence. There does not seem to lie any immediate possibilities for simplifications of the term in the block structure of the inactive density involved.

7 Future work

This implemented the MLHF second order geometry optimization was done in the AO basis. It would be highly desirable to further develop the method in the MO basis in such a way that a reduction in dimensions similar to that of the energy minimization can be achieved.

All the results obtained in this thesis have been obtained at the HF level of theory, but the MLHF geometry optimization method should be more extensively compared to other levels of theory, and to experimental results, in order to properly evaluate its performance.

The proof-of-concept calculations were only aimed at obtaining equilibrium geometries for benchmarking. Relatively small test systems were used due to problems with convergence for larger systems. Furthermore, the difference in size of the unfrozen and frozen regions were small, thus not representative of the massive size difference that would be present in target calculations. Lastly, there were no real chemical motivation behind the selection of the active spaces. Future studies to calculate chemical properties of larger systems with an appropriately selected active space with this method would be interesting.

This thesis has not been concerned with obtaining any results on the reduction in computation time for the MLHF method relative to the full space HF method. As the current implementation was only aimed at producing a code with the minimum necessary functionality, the computation times of the presented calculations are meaningless for this purpose. With a more streamlined and optimized implementation, the computational performance could be investigated.

Finally, further efforts to reduce the cost of the differentiated two-electron integral matrix should be attempted, e.g. by devising screening method for negligible interactions.

References

[1] Schlegel HB. Geometry optimization. WIREs Computational Molecular Science. 2011 Sep;1(5):790–809. Available from: https://onlinelibrary.wiley.com/doi/abs/10.1002/wcms.34.

[2] Townsend J, Kirkland JK, Vogiatzis KD. Post-Hartree-Fock methods: configuration interaction, many-body perturbation theory, coupled-cluster theory. In: Mathematical Physics in Theoretical Chemistry. Elsevier; 2019. p. 63–117. Available from: https://linkinghub.elsevier.com/retrieve/pii/B9780128136515000036.

[3] Helgaker T, Jørgensen P, Olsen J. Molecular Electronic-Structure Theory. Wiley; 2000. p. 433 – 481.

[4] Sousa SF, Ribeiro AJM, Neves RPP, Brás NF, Cerqueira NMFSA, Fernandes PA, et al. Application of quantum mechanics/molecular mechanics methods in the study of enzymatic reaction mechanisms. WIREs Computational Molecular Science. 2017 Mar;7(2). Available from: https://onlinelibrary.wiley.com/doi/abs/10.1002/wcms.1281.

[5] Ahmadi S, Barrios Herrera L, Chehelamirani M, Hostaš J, Jalife S, Salahub DR. Multiscale modeling of enzymes: QM-cluster, QM/MM, and QM/MM/MD: A tutorial review. International Journal of Quantum Chemistry. 2018 May;118(9):e25558. Available from: http://doi.wiley.com/10.1002/qua.25558.

[6] Tomasi J, Persico M. Molecular Interactions in Solution: An Overview of Methods Based on Continuous Distributions of the Solvent. Chemical Reviews. 1994 Nov;94(7):2027–2094. Available from: https://pubs.acs.org/doi/abs/10.1021/cr00031a013.

[7] Höfener S, Severo Pereira Gomes A, Visscher L. Molecular properties via a subsystem density functional theory formulation: A common framework for electronic embedding. The Journal of Chemical Physics. 2012 Jan;136(4):044104. Available from: http://aip.scitation.org/doi/10.1063/1.3675845.

[8] Hégely B, Nagy PR, Ferenczy GG, Kállay M. Exact density functional and wave function embedding schemes based on orbital localization. The Journal of Chemical Physics. 2016 Aug;145(6):064107. Available from: http://aip.scitation.org/doi/10.1063/1.4960177.

[9] Höfener S, Visscher L. Calculation of electronic excitations using wave-function in wave-function frozen-density embedding. The Journal of Chemical Physics. 2012 Nov;137(20):204120. Available from: http://aip.scitation.org/doi/10.1063/1.4767981.

[10] Warshel A, Levitt M. Theoretical Studies of Enzymic Reactions: Dielectric, Electrostatic and Steric Stabilization of the Carbonium Ion in the Reaction of Lysozyme. Journal of Molecular Biology. 1976;103:227–249.

[11] Senn HM, Thiel W. QM/MM Methods for Biomolecular Systems. Angewandte Chemie International Edition. 2009 Feb;48(7):1198–1229. Available from: http://doi.wiley.com/10.1002/anie.200802019.

[12] Svensson M, Humbel S, Froese RDJ, Matsubara T, Sieber S, Morokuma K. ONIOM: A Multilayered Integrated MO + MM Method for Geometry Optimizations and Single Point Energy Predictions. A Test for DielsAlder Reactions and Pt(P(t -Bu) $_3$) $_2$ + H $_2$ Oxidative Addition. The Journal of Physical Chemistry. 1996 Jan;100(50):19357–19363. Available from: https://pubs.acs.org/doi/10.1021/jp962071j.

[13] Vreven T, Morokuma K, Farkas Schlegel HB, Frisch MJ. Geometry optimization with QM/MM, ONIOM, and other combined methods. I. Microiterations and constraints. Journal of Computational Chemistry. 2003 Apr;24(6):760–769. Available from: http://doi.wiley.com/10.1002/jcc.10156.

[14] Wesolowski TA, Shedge S, Zhou X. Frozen-Density Embedding Strategy for Multilevel Simulations of Electronic Structure. Chemical Reviews. 2015 Jun;115(12):5891–5928. Available from: https://pubs.acs.org/doi/10.1021/cr500502v.

[15] Phillips JC, Kleinman L. New Method for Calculating Wave Functions in Crystals and Molecules. Physical Review. 1959 Oct;116(2):287–294. Available from: https://link.aps.org/doi/10.1103/PhysRev.116.287.

[16] Pernal K, Wesolowski TA. Orbital-free effective embedding potential: Density-matrix functional theory case. International Journal of Quantum Chemistry. 2009;109(11):2520–2525. Available from: http://doi.wiley.com/10.1002/qua.22016.

[17] Jacob CR, Neugebauer J. Subsystem density-functional theory: Subsystem density-functional theory. Wiley Interdisciplinary Reviews: Computational Molecular Science. 2014 Jul;4(4):325–362. Available from: http://doi.wiley.com/10.1002/wcms.1175.

[18] Lipparini F, Mennucci B. Perspective: Polarizable continuum models for quantum-mechanical descriptions. The Journal of Chemical Physics. 2016 Apr;144(16):160901. Available from: http://aip.scitation.org/doi/10.1063/1.4947236.

[19] Mennucci B. Continuum Solvation Models: What Else Can We Learn from Them? The Journal of Physical Chemistry Letters. 2010 May;1(10):1666–1674. Available from: https://pubs.acs.org/doi/10.1021/jz100506s.

[20] Miertus S, Scrocco E, Tomasi J. Electrostatic Interaction of a Solute with a Continuum. A Direct Utilization of Ab Initio Molecular Potentials for the Prevision of Solvent Effects. Chemical Physics. 1981;55:117–129.

[21] Klamt A, Schüürmann G. COSMO: a new approach to dielectric screening in solvents with explicit expressions for the screening energy and its gradient. J Chem Soc, Perkin Trans 2. 1993;(5):799–805. Available from: http://xlink.rsc.org/?DOI=P29930000799.

[22] Mata RA, Werner HJ, Schütz M. Correlation regions within a localized molecular orbital approach. The Journal of Chemical Physics. 2008 Apr;128(14):144106. Available from: http://aip.scitation.org/doi/10.1063/1.2884725.

[23] Li W, Piecuch P. Multilevel Extension of the Cluster-in-Molecule Local Correlation Methodology: Merging Coupled-Cluster and MøllerPlesset Perturbation Theories. The Journal of Physical Chemistry A. 2010 Jun;114(24):6721–6727. Available from: https://pubs.acs.org/doi/10.1021/jp1038738.

[24] Rolik Z, Kállay M. A general-order local coupled-cluster method based on the cluster-in-molecule approach. The Journal of Chemical Physics. 2011 Sep;135(10):104111. Available from: http://aip.scitation.org/doi/10.1063/1.3632085.

[25] Myhre RH, Sánchez de Merás AMJ, Koch H. Multi-level coupled cluster theory. The Journal of Chemical Physics. 2014 Dec;141(22):224105. Available from: http://aip.scitation.org/doi/10.1063/1.4903195.

[26] Dundas KOH. Density-Based Formulation of Multi-Level Hartree-Fock Theory. 2016;p. 51.

[27] Sæther S, Kjærgaard T, Koch H, Høyvik IM. Density-Based Multilevel Hartree–Fock Model. Journal of Chemical Theory and Computation. 2017 Nov;13(11):5282–5290. Available from: http://pubs.acs.org/doi/10.1021/acs.jctc.7b00689.

[28] Sæther S. Reduced orbital space coupled cluster calculations using a multilevel Hartree-Fock wave function. 2017;p. 51.

[29] Aidas K, Angeli C, Bak KL, Bakken V, Bast R, Boman L, et al. The Dalton quantum chemistry program system: The Dalton program. Wiley Interdisciplinary Reviews: Computational Molecular Science. 2014 May;4(3):269–284. Available from: http://doi.wiley.com/10.1002/wcms.1172.

[30] Folkestad SD, Kjønstad EF, Myhre RH, Andersen JH, Balbi A, Coriani S, et al. eT 1.0: An open source electronic structure program with emphasis on coupled cluster and multilevel methods. The Journal of Chemical Physics. 2020 May;152(18):184103. Available from: http://aip.scitation.org/doi/10.1063/5.0004713.

[31] Pulay P. Ab initio calculation of force constants and equilibrium geometries in polyatomic molecules: I. Theory. Molecular Physics. 1969 Jan;17(2):197–204. Available from: http://www.tandfonline.com/doi/abs/10.1080/00268976900100941.

[32] Pulay P. Analytical derivatives, forces, force constants, molecular geometries, and related response properties in electronic structure theory: Analytical calculation of energy derivatives. Wiley Interdisciplinary Reviews: Computational Molecular Science. 2014 May;4(3):169–181. Available from: http://doi.wiley.com/10.1002/wcms.1171.

[33] Bakken V, Helgaker T. The efficient optimization of molecular geometries using redundant internal coordinates. The Journal of Chemical Physics. 2002 Nov;117(20):9160–9174. Available from: http://aip.scitation.org/doi/10.1063/1.1515483.

[34] Murtagh BA, Sargent RWH. Computational experience with quadratically convergent minimisation methods. The Computer Journal. 1970 May;13(2):185–194.

[35] Pulay P. Convergence Acceleration of Iterative Sequences. The Case of SCF Iteration. Chemical Physics Letters. 1980;73(2):6.

[36] Császár P, Pulay P. Geometry Optimization by Direct Inversion in the Iterative Subspace. Journal of Molecular Structure. 1984;114:31–34.

[37] Helgaker T, Jørgensen P, Olsen J. Molecular Electronic-Structure Theory. Wiley; 2000. p. 80 – 89.

[38] Van Lenthe JH, Zwaans R, Van Dam HJJ, Guest MF. Starting SCF calculations by superposition of atomic densities. Journal of Computational Chemistry. 2006 Jun;27(8):926–932. Available from: http://doi.wiley.com/10.1002/jcc.20393.

[39] Høyvik IM. Convergence acceleration for the multilevel Hartree–Fock model. Molecular Physics. 2019 Jun;118(4):1626929. Available from: https://www.tandfonline.com/doi/full/10.1080/00268976.2019.1626929.

[40] Høst S, Olsen J, Jansík B, Thøgersen L, Jørgensen P, Helgaker T. The augmented Roothaan–Hall method for optimizing Hartree–Fock and Kohn–Sham density matrices. The Journal of Chemical Physics. 2008 Sep;129(12):124106. Available from: http://aip.scitation.org/doi/10.1063/1.2974099.

[41] Helgaker T, Jørgensen P. Analytical Calculation of Geometrical Derivatives in Molecular Electronic Structure Theory. In: Advances in Quantum Chemistry. vol. 19. Elsevier; 1988. p. 183–245. Available from: https://linkinghub.elsevier.com/retrieve/pii/S0065327608606164.

[42] Olsen J, Bak KL, Ruud K, Helgaker T, Jorgensen P. Orbital connections for perturbation-dependent basis sets. 1995;p. 19.

[43] Lindh R, Bernhardsson A, Karlström G, Malmqvist P On the use of a Hessian model function in molecular geometry optimizations. Chemical Physics Letters. 1995 Jul;241(4):423–428. Available from: https://linkinghub.elsevier.com/retrieve/pii/000926149500646L.

[44] Eckert F, Pulay P, Werner HJ. Ab initio geometry optimization for large molecules. Journal of Computational Chemistry. 1997 Sep;18(12):1473–1483. Available from: http://doi.wiley.com/10.1002/%28SICI%291096-987X%28199709%2918%3A12%3C1473%3A%3AAID-JCC5%3E3.0.CO%3B2-G.

[45] Pulay P, Fogarasi G. Geometry optimization in redundant internal coordinates. The Journal of Chemical Physics. 1992 Feb;96(4):2856–2860. Available from: http://aip.scitation.org/doi/10.1063/1.462844.

[46] Wang LP, Song C. Geometry optimization made simple with translation and rotation coordinates. The Journal of Chemical Physics. 2016 Jun;144(21):214108. Available from: http://aip.scitation.org/doi/10.1063/1.4952956.

[47] Peng C, Ayala PY, Schlegel HB, Frisch MJ. Using redundant internal coordinates to optimize equilibrium geometries and transition states. Journal of Computational Chemistry. 1996 Jan;17(1):49–56. Available from: http://doi.wiley.com/10.1002/%28SICI%291096-987X%2819960115%2917%3A1%3C49%3A%3AAID-JCC5%3E3.0.CO%3B2-0.

[48] Fogarasi G, Zhou X, Taylor PW, Pulay P. The calculation of ab initio molecular geometries: efficient optimization by natural internal coordinates and empirical correction by offset forces. Journal of the American Chemical Society. 1992 Oct;114(21):8191–8201. Available from: https://pubs.acs.org/doi/abs/10.1021/ja00047a032.

[49] Pulay P. Ab initio calculation of force constants and equilibrium geometries in polyatomic molecules: II. Force constants of water. Molecular Physics. 1970 Apr;18(4):473–480. Available from: http://www.tandfonline.com/doi/abs/10.1080/00268977000100541.

[50] DeFrees DJ, Raghavachari K, Schlegel HB, Pople JA. Effect of Electron Correlation on Theoretical Equilibrium Geometries. 2. Comparison of Third-Order Perturbation and Configuration Interaction Results with Experiment. American Chemical Society. 1982;104(21):5.

[51] Helgaker T, Gauss J, Jo/rgensen P, Olsen J. The prediction of molecular equilibrium structures by the standard electronic wave functions. The Journal of Chemical Physics. 1997 Apr;106(15):6430–6440. Available from: http://aip.scitation.org/doi/10.1063/1.473634.

[52] Teale AM, Tozer DJ. Ground- and excited-state diatomic bond lengths, vibrational levels, and potential-energy curves from conventional and localized Hartree–Fock-based density-functional theory. The Journal of Chemical Physics. 2005 Jan;122(3):034101. Available from: http://aip.scitation.org/doi/10.1063/1.1824892.

[53] Csonka GI, Sztraka L. Density functional and post Hartree-Fock equilibrium geometries, potential energy surface and vibrational frequencies for methylamine. Chemical Physics Letters. 1995 Feb;233(5-6):611–618. Available from: https://linkinghub.elsevier.com/retrieve/pii/000926149401504O.

[54] Xie Y, Scuseria GE, Yates BF, Yamaguchi Y, Schaefer HF. Methylnitrene; theoretical predictions of its molecular structure and comparison with the conventional C-N single bond in methylamine. Journal of the American Chemical Society. 1989 Jul;111(14):5181–5185. Available from: https://pubs.acs.org/doi/abs/10.1021/ja00196a026.

[55] Larsen H, Helgaker T, Olsen J, Jørgensen P. Geometrical derivatives and magnetic properties in atomic-orbital density-based Hartree–Fock theory. The Journal of Chemical Physics. 2001;115(22):10344. Available from: http://scitation.aip.org/content/aip/journal/jcp/115/22/10.1063/1.1415082.

[56] Hanwell MD, Curtis DE, Lonie DC, Vandermeersch T, Zurek E, Hutchison GR. Avogadro: an advanced semantic chemical editor, visualization, and analysis platform. Journal of Cheminformatics. 2012 Dec;4(1). Available from: https://jcheminf.biomedcentral.com/articles/10.1186/1758-2946-4-17.

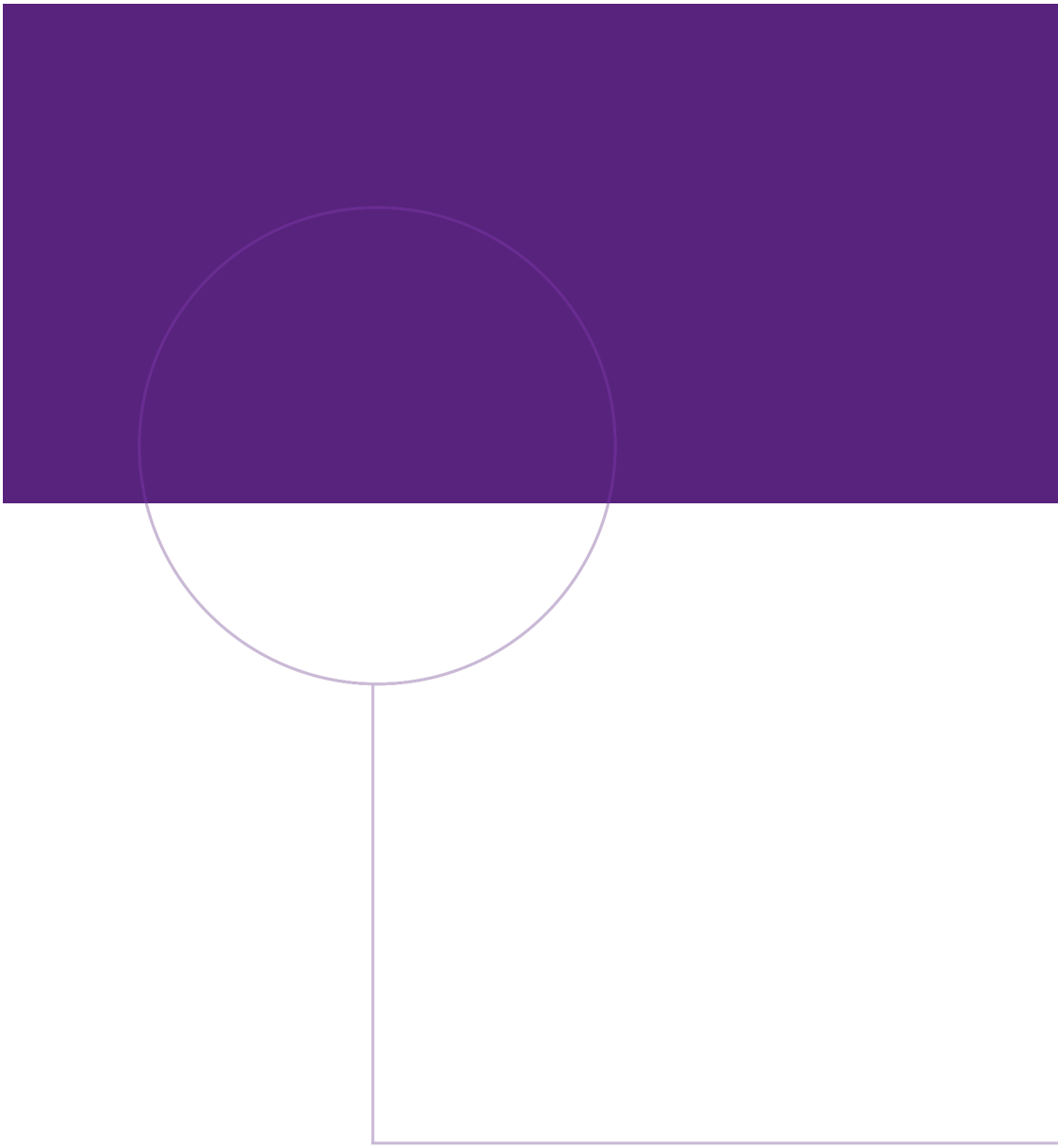

NTNU

Norwegian University of
Science and Technology